Influence of confinement on the dissolution of carbon dioxide in a vertical cylindrical cell

Daniël P. Faasen,* Detlef Lohse,† and Devaraj van der Meer‡
Physics of Fluids Group, Faculty of Science and Technology, University of Twente, 7500 AE Enschede, The Netherlands

(Received 29 May 2024; accepted 17 September 2024; published 24 October 2024)

If carbon dioxide dissolves into a body of water, a CO_2-rich boundary layer forms at the interface, which is denser in comparison to pure water. Continued dissolution of CO_2 into the water barrier results in the layer becoming gravitationally unstable, leading to the onset of buoyancy-driven convection and, consequently, the shedding of a buoyant plume. In this work, we look at the influence of confinement on this process in two ways: In the first part we focus on expanding our understanding of the short-time, transient diffusion of CO_2 into a vertical water barrier confined to a narrow cylindrical cell by varying the cylinder diameter and CO_2 pressure. By adding sodium fluorescein, a pH-sensitive fluorophore, we directly visualize the dissolution and propagation of the CO_2 across the liquid barrier. Combined with particle-tracking experiments we quantify the effects of the cylinder width and CO_2 pressure on the initial diffusive behavior, the onset of convection, and the enhancement of the buoyancy driven convection of the subsequent transport. In the second part, we investigate the long-time, steady mass transfer dynamics in the liquid barrier by trapping a slug bubble underneath the liquid barrier and varying the barrier height and partial CO_2 pressure. We find that initially the Sherwood number scales as $\mathrm{Sh} \propto \mathrm{Ra}^{1/4}$ with the Rayleigh number Ra, but for a sufficiently large barrier the Sherwood number reaches a constant value. Building on the ideas of Ahlers *et al.* [Phys. Rev. Lett. **128**, 084501 (2022)], rescaling the Rayleigh number with an aspect-ratio-dependent relevant length scale results in a universal Sh vs Ra dependence.

DOI: 10.1103/PhysRevFluids.9.103501

I. INTRODUCTION

The carbon dioxide concentration in the atmosphere has been steadily increasing since the start of the industrial revolution and despite efforts to lower emissions, does not show any sign of stabilizing or decreasing in the near future [1]. Carbon capture and utilization could help to close the gap in the carbon cycle by capturing CO_2 before or after it has been emitted into the atmosphere and then either processing it into useful chemicals [2] or injecting it into deep saline aquifers, trapping the CO_2 between a layer of cap rock and a liquid reservoir, resulting in the long-term storage of the CO_2 in the reservoir [3–5]. However, this does require a thorough understanding of the dissolution and subsequent mass transfer of carbon dioxide gas into liquid barriers.

When carbon dioxide comes into contact with a water barrier and starts to dissolve into it, a CO_2-rich boundary layer forms at the gas-water interface, which is denser in comparison to pure water. While initially stable, the continued dissolution of CO_2 into the water layer results in the

*Contact author: daniel.p.faasen@gmail.com
†Contact author: d.lohse@utwente.nl
‡Contact author: d.vandermeer@utwente.nl

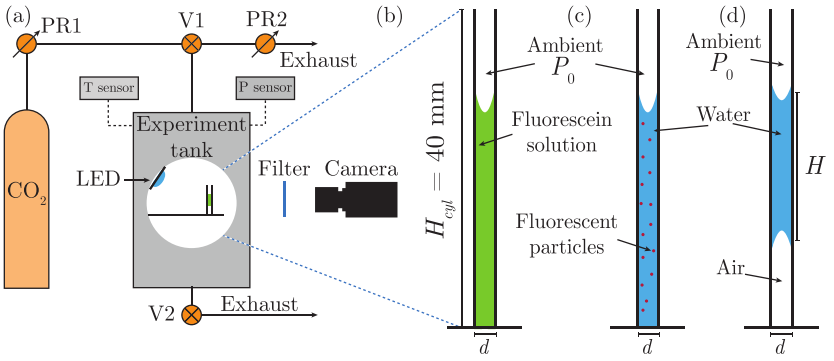

FIG. 1. (a) Schematic overview of the experimental setup. (b) Sketch of the cylinder prepared for the fluorescence experiments, (c) particle-tracking velocimetry experiments, and (d) for the bubble growth experiments.

CO_2-rich fluid layer becoming gravitationally unstable, leading to the onset of buoyancy-driven convection and the shedding of buoyant plumes, which greatly enhances both the mass transfer of CO_2 into the water layer from the gas phase and that within the water layer itself [6,7]. In addition, if the reservoir is closed, the pressure in the CO_2-rich gas phase above the brine will decay over time, which leads to a reduction in the convective dissolution rate even before the brine is saturated with CO_2 [8]. Furthermore, density-driven convection can also occur as a result of buoyancy generating chemical reactions [9–12], droplet dissolution [13,14], and bubble growth [15,16].

Studies investigating the dissolution and propagation dynamics of CO_2 in water barriers mainly focus on the onset of the density-driven convection, the subsequent propagation and mixing dynamics, and the resulting mass transfer rate [17–22]. It is, for example, well known and understood that the onset of the density-driven convection occurs earlier in less confined systems [17,23–25,34]. Furthermore, after the onset of convection, diffusive behavior is observed, albeit with a much higher effective diffusion coefficient [18,19,26]. Depending on the experimental conditions, this effective diffusion coefficient can be several orders of magnitude larger in comparison to the expected diffusive counterpart under similar experimental conditions [20–22,27,28]. Consequently, the mixing rate and mass transfer rate are also strongly dependent on the geometry of the system investigated.

In the first part of this work we focus on expanding our understanding of the short-time, transient diffusion of CO_2 into a vertical water barrier confined to a narrow cylindrical cell, as shown in Fig. 1, by varying the cylinder diameter and CO_2 pressure. We replace the ambient air atmosphere with a CO_2 atmosphere and by adding sodium fluorescein, a pH-sensitive fluorophore, to the liquid barrier, we can directly visualize the propagation of CO_2 [29–32]. Combined with particle tracking, we can study the influence of the cylinder diameter and CO_2 pressure on the initial diffusive behavior, the onset of convection, and the enhancement of the buoyancy-driven convection of the subsequent transport. In the second part, we investigate the long-time, steady mass transfer dynamics in the liquid barrier by trapping a slug bubble underneath the liquid barrier and varying the barrier height and (partial) CO_2 pressure [33]. Note that in both parts we essentially study the influence of *confinement* on the dissolution of CO_2 into the cylinder, by changing the aspect ratio of the cell (through either its diameter or height) and the driving force (varying the CO_2 pressure).

In summary, our aim is to investigate the influence of the experimental settings on the short-time, transient diffusion and long-time, steady mass transfer dynamics of CO_2 into a liquid barrier. Varying the CO_2 pressure will vary the strength of buoyancy-driven convection while varying the cylinder diameter varies the influence of viscosity which counteracts the buoyancy-driven convection. By defining the aspect ratio based on the cylinder diameter and CO_2 front position, $\Gamma = d/z_f$, the critical Rayleigh number can be predicted using theory developed for Rayleigh-

Bénard convection [25,34]. Furthermore, Taylor-Aris dispersion is used to predict the effective diffusion coefficient. Finally, we quantify the long-term mass transfer rates in the slug bubble growth experiments by obtaining the Sherwood number. We show that the results can be collapsed by rescaling the Rayleigh number by a relevant length scale which is dependent on the aspect ratio, in which the full barrier height is taken into account.

This paper is organized as follows. The experimental setup and procedures are described in Sec. II. In section III we present the effects of the cylinder diameter and partial CO_2 pressure on the short-time, transient diffusion of CO_2 into the liquid barrier based on the fluorescence and particle-tracking experiments. In Sec. IV we show the influence of the barrier height and partial CO_2 pressure on the long-time, steady mass transfer dynamics in the liquid barrier using the bubble growth experiments. The paper ends with a summary of the main findings and an outlook in Sec. V.

II. EXPERIMENTAL PROCEDURE

A schematic overview of our experimental setup is shown in Fig. 1(a). The experiments are conducted inside a sealed chamber which can be flushed and pressurized with CO_2 gas. The inlet pressure can be changed between 1.0 bar and 5.0 bar using the pressure regulator PR1, whereas pressure regulator PR2 prevents over-pressurization of the experimental tank. Inside the chamber, a pressure and temperature sensor record the time dependence of the pressure $P_0(t)$ and temperature $T(t)$, respectively (1 acquisition per second). A more detailed description of the experimental chamber and pressure control system can be found elsewhere [35].

A single borosilicate glass (Duran) cylinder is attached on one end to a silicon wafer plate using Loctite 4305 (Farnell), in an almost perfectly vertical manner, while the other end is left open. The cylinder is positioned under a small and unavoidable tilt angle, which has a significant influence on both the timing of and the way in which the onset of convection takes place, which was highlighted in previous work [32]. Cylinders of varying inner diameters are used, ranging from $d = 1.0$ mm to 5.0 mm, all with a height of 40 mm. Before use, the cylinders are rinsed using ethanol (Boom, technical grade) followed by Milli-Q water (resistivity = 18.2 MΩ cm) and finally dried in a nitrogen stream.

We use three different techniques in order to study the dissolution and subsequent transport of CO_2 through the liquid barrier. (i) We perform fluorescence experiments to study the short-time, transient diffusion of CO_2 into the liquid barrier, in particular the initial diffusive behavior and the onset of convection. (ii) Particle-tracking velocimetry experiments are performed to determine the velocities in the early convective stage. Finally, (iii) we perform bubble growth experiments to study the long-time, steady mass transfer dynamics in the liquid barrier. Therefore, we prepare the cylinders in one of three different configurations depending on the experiment. A detailed description for each is provided below.

A. Fluorescence experiments

For the fluorescence experiments we use cylinders of varying inner diameter, ranging from $d = 1.0$ mm to $d = 5.0$ mm. A layer of a 10^{-4} M aqueous fluoroscein solution is injected into the cylinders, at a volume corresponding to a barrier height of $H \approx 28$ mm (e.g., $V = 200$ µl for $d = 3.0$ mm), which acts as the liquid barrier; see Fig. 1(b). This solution is freshly prepared prior to the experiments by adding sodium fluorescein salt (Fisher Scientific, general purpose grade) to Milli-Q water. Fluoroscein is a well-known fluorophore often used in biological applications, with its main absorbance peak at 490 nm and main emission peak at 513 nm [29–31]. More importantly, the emission intensity of fluorescein has a (nonlinear) dependency on the pH level of the liquid, allowing us to follow the dissolution and propagation of the CO_2 in the liquid. Furthermore, the presence of the sodium fluorescein in the barrier does not affect the diffusive and convective behavior of the CO_2, as for example we only need ∼7.3 µg sodium fluorescein in a 200 µl barrier to achieve the desired concentration.

Inside the tank, a LED (Thorlabs, $\lambda_{\text{center}} = 470$ nm) is located to illuminate the cylinder. We use a Nikon D850 camera in silent interval timer shooting mode (1 fps) in combination with a Zeiss Makro Planar T 100 mm lens to achieve a mean optical resolution of 10.4 μm/pixel. In the optical path between the cylinder and the camera, a bandpass filter (Thorlabs, $\lambda_{\text{center}} = 530$ nm, BW = 43 nm) is located to filter out the LED light.

After preparation, the cylinder is placed inside the experimental chamber. The fluorescent experiments are conducted in one of either two ways, with or without a flushing stage. In both cases the experiment starts by turning on the LED inside the chamber, followed 5 s later by the activation of the interval timer shooting mode on the camera. Fifteen seconds after camera activation, the pressure and temperature sensor data starts being recorded. In case of experiments with a flushing stage, 35 s after turning on the LED, valve V1 is opened and the system is flushed with CO_2 gas in order to fully replace the ambient air inside the tank. The time at the start of the flushing stage is $t = 0$ s and marks the start of the "experiment" stage. After flushing for 60 s, the tank is pressurized to the pressure level of the experiment.

In case of experiments without the flushing stage, 35 s after turning on the LED the tank is immediately pressurized to the pressure level of the experiment. Therefore this point marks $t = 0$ s, the start of the "experiment" stage. As a result of not flushing the tank, 1.0 bar of air remains inside the tank. At the end of all experiments (typically at $t = 15$ min), the experimental tank is opened and flushed using a nitrogen spray gun to prepare the experimental chamber for the next experiment.

B. Particle-tracking velocimetry experiments

For the particle-tracking velocimetry (PTV) experiments a similar protocol to the fluorescence experiments is followed. The inner diameter of the cylinders used vary between $d = 2.0$ mm and $d = 5.0$ mm. The cylinder with an inner diameter of $d = 1.0$ mm is not used in the PTV experiments, since the size of the particles used would make measurements unreliable. The liquid barrier, again of height $H \approx 28$ mm, now consists of a layer of Milli-Q water seeded with fluorescent red polyethylene microspheres (Cospheric). The microparticles have a diameter between 125 and 150 μm, are neutrally buoyant ($\rho_{\text{particle}} = 995$ kg/m^3), absorb light between 300–550 nm, and have an emission peak around 607 nm. Since polyethylene particles are hydrophobic, they have been supplied suspended in an aqueous solution of 0.1% Tween 20 surfactant and deionized water. This solution is further diluted using Milli-Q water, such that we find ∼15 particles in the liquid barrier; see Fig. 1(c).

The characteristic response time of the particles is its Stokes time,

$$\tau_p = \frac{d_p^2 \Delta\rho}{18\mu}, \tag{1}$$

where $d_p = 125$–150×10^{-6} m is the diameter of the particles, $\Delta\rho = \rho_w - \rho_{\text{particle}} = 2.77$ kg/m^3 the density difference between the water and the particles, and $\mu = 9.5 \times 10^{-4}$ Ns/m^2 is the dynamic viscosity of the water at 295 K [36]. We find a characteristic response time in the order of microseconds, which indicates that these particles are very suitable to study the flow in our system.

We follow the same experimental protocol as described for the fluorescence experiments with the flushing stage. However, the LED inside the tank and the bandpass filter in the optical path have been replaced by another LED (Thorlabs, $\lambda_{\text{center}} = 530$ nm) and filter (Thorlabs, $\lambda_{\text{center}} = 630$ nm, BW = 69 nm), corresponding to the absorption and emission wavelengths of the microparticles.

C. Bubble growth experiments

The bubble growth experiments are conducted using only the cylinder with an inner diameter of $d = 3.0$ mm. A layer of pure Milli-Q water is injected into the cylinder at a volume ranging between $V = 30$ μl and $V = 200$ μl, which acts as the liquid barrier. As a result, the barrier height varies between $H_w = 4.2$ mm to 28 mm. Using an air-filled syringe, a bubble is injected between the

plate wall and the injected water barrier, as depicted in Fig. 1(d). The bubble is held in place due to a stable balance between the weight of the water barrier and a combination of the surface tension of the water-bubble interface and to a lesser extent the differences in gas pressure. This force balance persists during the experiments, since the surface tension of CO_2 on water is almost the same as the surface tension of air on water under our experimental conditions [37].

Instead of using an LED inside the tank to illuminate the cylinder during these experiments, we use a Schott KL2500 LED light source located outside of the experimental chamber. Furthermore, the Nikon D850 camera, while still operating in silent interval timer shooting mode, now operates at 1/30 fps, as the experimental time frame is shifted to 1.5 hr. Similar to the fluorescence experiments, we start by activating the interval timer shooting mode on the camera. Fifteen seconds after camera activation, the pressure and temperature sensor data starts being recorded. Finally, 30 s after stating the camera, the flushing stage is started. After flushing for 60 s, valve V2 is closed and the inlet pressure is set to the pressure level of the experiment, ranging from 1.0 to 4.0 bar. In the bubble growth experiments the end of the flushing cycle marks the start of the experiments at $t = 0$ s, in contrast to the fluorescence experiments in which the start of the flushing stage marks the start of the experiments.

If the experiments are conducted above atmospheric pressure, the bubble volume compresses at the moment of pressurisation as established by Boyle's law. As a result, the reference bubble volume is taken to be V_f, the volume of the bubble after pressurisation, which in these experiments is tuned to $V_f = 30$ µl. This is justified provided that any changes in the molar gas contents in the bubble (initially air) remain negligible during the flushing stage, i.e., under the assumption that there is insignificant mass transfer to or from the bubble up to that point, which we have shown in earlier work to be the case [33]. Furthermore, experiments have also been conducted using a gas mixture prepared in an external tank, consisting of 50% N_2 and 50% CO_2 gas. We obtained this gas mixtures by mixing an equal volume of N_2 and CO_2 gas in the external tank. This mixture is injected in a similar manner as previously described, resulting in the experiment being conducted at a partial CO_2 pressure of ∼0.5 bar. At the end of the experiment (typically at $t = 90$ min), the experimental tank is opened and flushed using a nitrogen spray gun to prepare the experimental chamber for the next experiment.

III. SHORT-TIME, TRANSIENT DIFFUSION OF CO_2 INTO THE LIQUID BARRIER

A. Influence of the cylinder width

We start by investigating the influence of the cylinder width on the onset of convection and the propagation dynamics of the CO_2 front. Therefore, we analyze a series of fluorescence experiments, with inner cylinder diameters of $d = 1.0$, 2.0, 2.4, 3.0, 4.0, and 5.0 mm at a pressure of $P_{CO_2} = 1.0$ bar. Figure 2 shows snapshots of a selection of these experiments. As the CO_2 starts dissolving into the liquid barrier, the pH of the CO_2 infused liquid starts to decrease. Since fluorescein is a pH-sensitive fluorophore in the pH range between 5 and 10, the emission intensity of the fluorescein dye starts to decrease, resulting in a color change of the dye from bright green to black in the images [38].

At the beginning of the experiments, $t = 0$ s, we start replacing the air atmosphere in the chamber with a CO_2 atmosphere. Almost immediately, CO_2 starts dissolving into the liquid barrier, forming a CO_2-rich water layer just below the gas-liquid interface. While initially stable, the continued dissolution of CO_2 into the water barrier results in the layer becoming gravitationally unstable, since the CO_2-rich water is denser in comparison to the pure water underneath. Once this happens, a convective plume is shed from the CO_2-rich boundary layer which starts propagating downwards into the liquid barrier.

For the experiments shown in Fig. 2, it is clear that the width of the cylinder has a significant impact on the dissolution and propagation dynamics of the CO_2 through the liquid barrier. For experiment (i), with inner diameter $d = 2.0$ mm, it almost appears as if convection does not set in

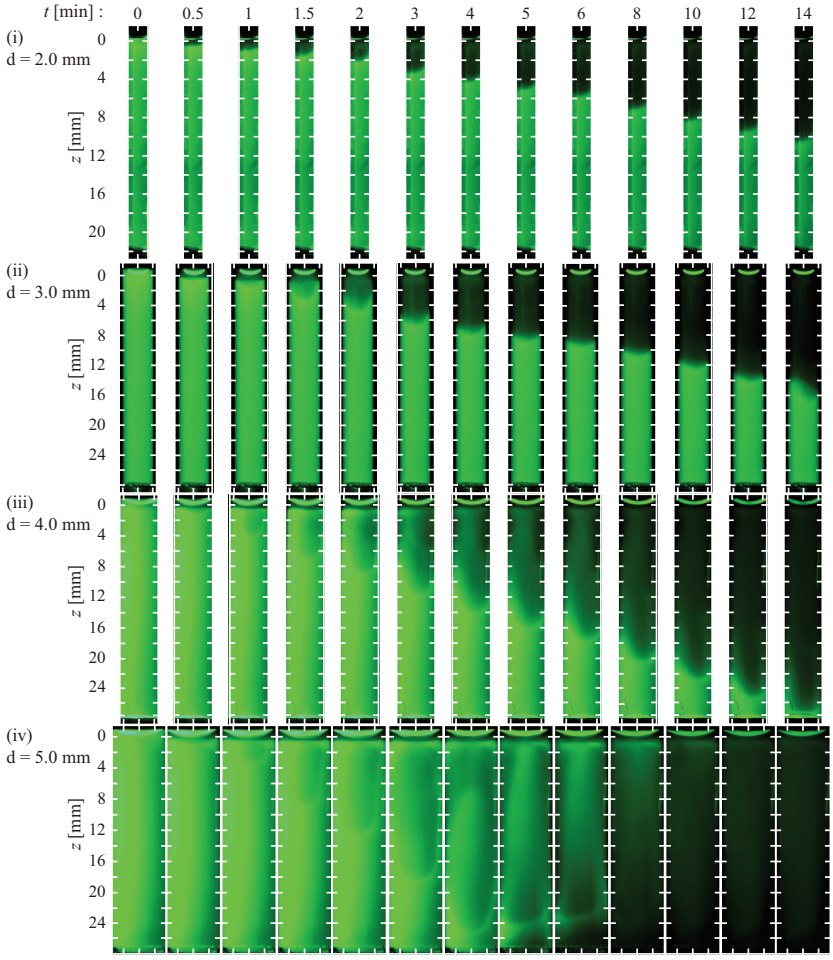

FIG. 2. Fluorescence images of the initial dissolution process of CO_2 in a vertical liquid column within a cylindrical cell of different inner diameters. In (i) the inner diameter $d = 2.0$ mm, for (ii) $d = 3.0$ mm, for (iii) $d = 4.0$ mm, and for (iv) $d = 5.0$ mm. The fluorescence intensity decays with pH or increasing CO_2 concentration. At $t = 0$, the upper interface is exposed to a CO_2 gas ambient. Subsequently, a CO_2-containing layer (dark region) propagates downwards.

at all and the front progresses downwards diffusively. Only a small plume observable around $t \sim 1.5$ min suggests that convection has set in. As the cylinder diameter increases, the onset of convection become more apparent and appears to occur earlier. In experiment (ii), inner diameter $d = 3.0$ mm, the onset occurs around $t \sim 1.0$ min while for inner diameter $d = 4.0$ mm and 5.0 mm, the onset appears to occur already around $t \sim 30$ s. Moreover, the boundary layer thickness at the onset decreases as the cylinder width increases.

After the onset of convection, further differences in the propagation dynamics can be observed. In (i) and (ii) the propagation of the CO_2 appears to be axisymmetric and very stable. At the very end of (ii) this axisymmetry is broken, resulting in the shedding of a lateral buoyant upwelling plume. As a result, the CO_2 front accelerates to a higher velocity, leading to the front reaching the bottom interface faster in comparison to experiments in which the shedding of the upwelling plume does not occur [32]. For (iii) and (iv), the CO_2 front appears to initially propagate downward on the right side of the cylinder, while the left side remains unaffected. In (iii) the front eventually

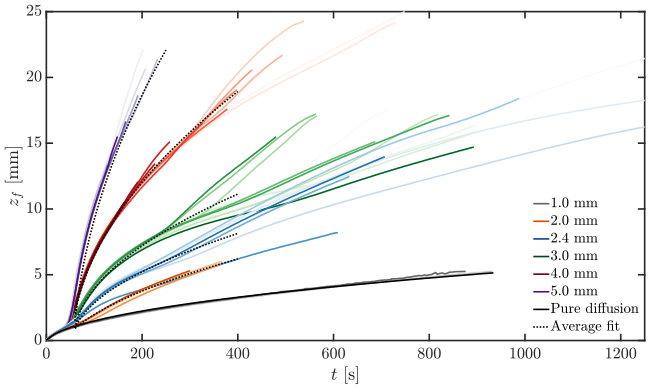

FIG. 3. Front trajectory $z_f(t)$ corresponding to the 85% intensity threshold of the horizontally averaged intensity profiles, namely, $\overline{I}^*(z_f, t) = 0.85$. The front trajectory of all experiments vs time are plotted for the varying cylinder widths d . The black dotted lines show the best fit of Eq. (8) after the onset of convection.

becomes axisymmetric around $t \sim 5$ min, although the tip of the CO_2 front remains on the right side of the cylinder. For the widest cylinder in (iv), the front does not stabilize at all before it reaches the bottom of the cylinder. Furthermore, a clear convective roll is visible, in which CO_2-rich liquid is transported downwards on the right side of the cylinder, while pure liquid is transported upward on the left side of the cylinder. Once the CO_2 has reached the bottom, the CO_2 evenly spreads throughout the barrier and fully darkens the liquid.

To further quantify the propagation dynamics, we extract the position of the front as a function of time from the snapshots. We start from the measured intensities $G(x, z, t)$, which can be seen as the integral of the intensities of the fluorescent particles over the path of view, i.e., with more fluorescent particles participating to the signal in the center of the cylindrical cell as on the side. Subsequently, these measured intensities are summed in the horizontal (x) direction, which then lead to integrated intensities $G(z, t)$ which are then a function of depth z and time t only and correspond to the integrated intensity over a horizontal cross section of the cell. We normalize the obtained intensities with respect to the initial intensity profile in order to account for spatial inhomogeneity of the LED lighting in the chamber, defined as the normalized intensity $I = G(z, t)/G(z, 0)$. Additionally, the intensity profiles are corrected for the decay in intensity due to photobleaching of the fluorescein. Finally, we once more normalize the obtained intensities by the maximum and minimum obtained intensities of the experiments, resulting in $\overline{I}^*(z_f, t)$. A more detailed explanation of this process can be found in our previous work [32]. We define the position of the CO_2 front, $z_f(t)$, as the 85% intensity threshold of the horizontally averaged intensity profiles, $\overline{I}^*(z_f, t) = 0.85$. A detailed explanation and justification of this procedure can also be found in [32]. Tracing this position in time yields Fig. 3, which shows the front trajectories of all experiments vs time for the varying cylinder widths.

As explained before, the dissolution of CO_2 into the liquid barrier results in the formation of a CO_2-rich boundary layer at the top interface. The mass transport in this layer is purely driven by diffusion and therefore the propagation of the front z_f(t) follows the self-similar solution for pure diffusion:

$$\frac{C(z,\ t)}{C_{\text{sat}}} = \text{erfc}\left(\frac{z}{\sqrt{4Dt}}\right), \tag{2}$$

where $C(z,\ t)$ is the local CO_2 concentration and C_{sat} is the saturation concentration of CO_2 in water. The front trajectory associated to concentration C_f is thus

$$z_f = K_f\sqrt{Dt_f}, \tag{3}$$

where growth prefactor K_f depends on the concentration

$$K_f \equiv 2\mathrm{erfc}^{-1}(C_f/C_{\mathrm{sat}}). \tag{4}$$

In Fig. 3 the solid black line,which is almost coincidental with the data for $d = 1.0$ mm, follows from Eqs. (3) and (4), taking $K_f \equiv 2\mathrm{erfc}^{-1}(C_f/C_{\mathrm{sat}}) = 4.85$ corresponding to $C_f/C_{\mathrm{sat}} = 5.8 \times 10^{-4}$ ($I^* = 0.85$), which we obtained from the calibration curve in Ref. [32]. We see that the experiments initially follow the self-similar solution until the onset of convection. Additionally, we observe that for the cylinder with an inner diameter of $d = 1.0$ mm convection never sets in and the propagation of the front remains purely diffusive throughout the entire experiment.

For the cylinders with a larger diameter, we observe a sharp acceleration of the CO_2-front position after the onset of convection, due to the shedding of the buoyant plume. Given the incompressibility of the fluid, the induced convective flow can not affect the mean interface position. It does, however, lead to a heavy distortion of the front, visible in Fig. 2, leading to a significant increase in the surface area of the front. This results in an increase of the concentration gradients across the CO_2 front, as the lateral diffusive fluxes across the interface become nonzero, which leads to the increase in front propagation velocity. These increased lateral diffusive fluxes also drive the reflattening process of the CO_2 front and eventually an equilibrium is reached between the advective distortion of the CO_2 front and the diffusive fluxes. The front trajectory after the onset can still be described with a relation similar to the analytical solution of a pure diffusive problem, albeit with an effective diffusion coefficient. For example, for a cylinder with an inner diameter of $d = 3.0$ mm, we found this effective diffusion coefficient to be 8.5 times higher than expected for CO_2 in water [32]. The effective diffusion coefficients for all cylinder widths will be obtained and discussed in Sec. III D.

B. Influence of the CO_2 pressure

We continue by investigating the influence of the (partial) CO_2 pressure inside the chamber on the onset of convection and the propagation dynamics of the CO_2 front in a similar fashion as we did for the influence of the cylinder width. We vary the CO_2 pressure between $P_{CO_2} = 1.0$ and 5.0 bar. Since the onset of convection occurs before the flushing stage ends, we perform the experiments with and without the flushing stage to investigate whether this affects our measurements. It should be noted that, in the case of no-flush experiments, 1.0 bar of air remains in the chamber and are thus conducted at a total pressure of $P_0 = P_{CO_2} + 1.0$ bar. We will show that, as expected, the presence of the 1.0 bar of air does not affect the experiments.

Figure 4 shows snapshots of a selection of pressure experiments, with P_{CO_2} starting at 1.0 bar for (v) and increasing to 4.0 bar for (viii), performed without the flushing stage. For experiment (v), the onset of convection occurs around $t \sim 1.0$ min, as previously observed. For experiments (vi)–(viii), the onset of convection appears to occur earlier and in all three experiments has already occurred before the $t \sim 30$ s frame. Furthermore, while the front propagation remains stable and seemingly asymmetric in all four cases, the propagation velocity clearly increases with an increase in CO_2 pressure. This is due to the barrier being able to take up more CO_2 at higher pressures, as it follows from Henry's law. Consequently, the concentration gradients at the top interface increases at increased CO_2 pressure, resulting in more CO_2 dissolving into the liquid barrier at a faster rate. As a result, the CO_2-rich boundary layer becomes unstable earlier as the CO_2 pressure increases, resulting in an earlier shedding of the buoyant plume, which in turn is driven downwards faster due to the increased concentration gradients at the top interface.

As before, we extract the front position from the images and obtain Fig. 5 which shows the front trajectories of the pressure experiments conducted with the flushing stage (solid, colored lines) and without the flushing stage (dashed, colored lines) vstime. The trajectories are offset by the onset time t_1, defined as the point in time between where the front velocity, $\mathrm{d}z_f/\mathrm{d}t$, is minimum and the front acceleration, $\mathrm{d}^2z_f/\mathrm{d}t^2$, is maximum, and corresponding front position $z_f(t_1) = z_1$. Offsetting

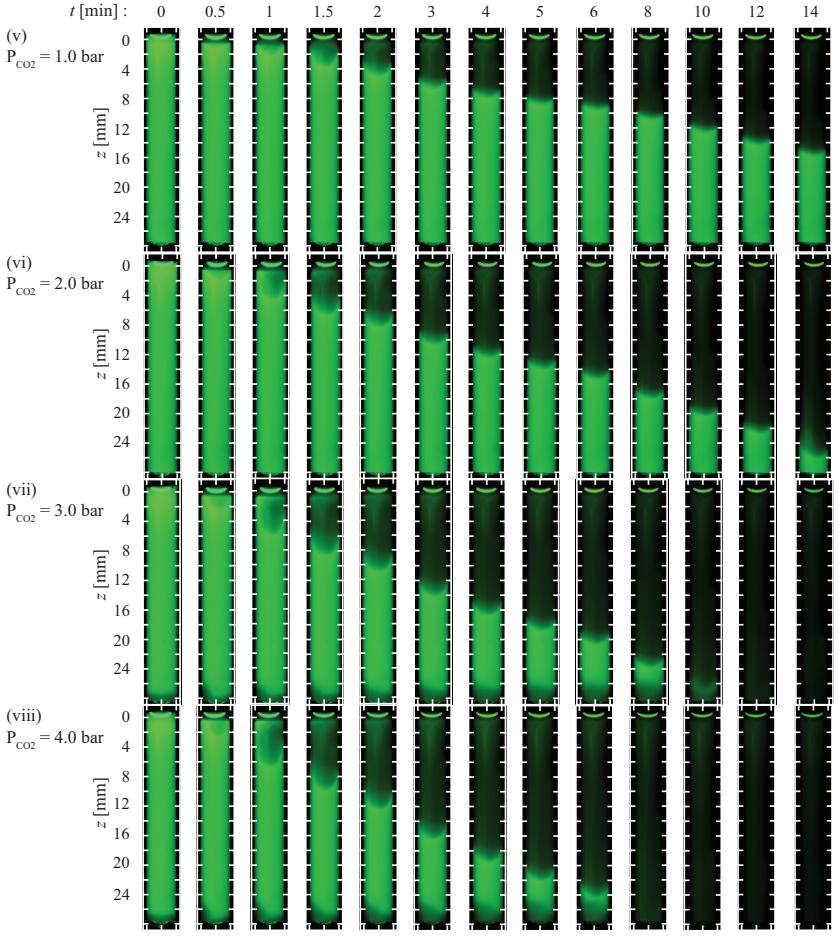

FIG. 4. Fluorescence images of the initial dissolution process of CO_2 in a vertical liquid column within a cylindrical cell of inner diameter $d = 3.0$ mm at different pressures without the flushing stage. In (v) the CO_2 pressure is $P_{CO_2} = 1.0$ bar, for (vi) $P_{CO_2} = 2.0$ bar, for (vii) $P_{CO_2} = 3.0$ bar, and for (viii) $P_{CO_2} = 4.0$ bar.

the front trajectories by t_1 and z_1 allows for a fair comparison between the experiments with and without the flushing stage.

Figure 5 proves that the flushing stage does not influence the CO_2 propagation dynamics and neither does the presence of 1.0 bar or air in the no-flush experiments. The main difference between the experiments with and without the flushing stage is found during the initial, purely diffusive stage prior to the onset of convection. For $P_{CO_2} = 1$ bar, the experiments are very comparable and the onset of convection occurs at almost the same time. However, for higher pressure experiments, the onset of convection in the no-flush experiments always occurs earlier than $t = 60$ sec, which in the experiments with a flushing stage would be during the flushing of the chamber. Therefore, the no-flush experiments are preferred, as they provide the more reliable onset time and depth for the different pressures. Furthermore, the increase in front propagation velocity observed in the snapshots is highlighted in Fig. 5, which as explained above is due to the increased concentration gradients driving the front propagation. Moreover, the observed convective behavior can again be described with the analytical solution of a pure-diffusion problem with an effective diffusion coefficient, which will be performed in Sec. III D.

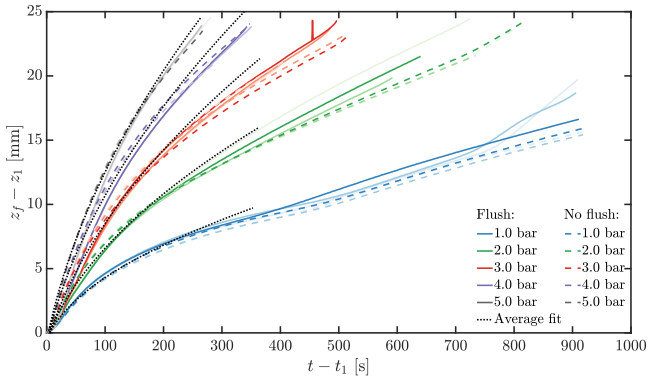

FIG. 5. Front trajectory $z_f(t)$ corresponding to the 85% intensity threshold of the horizontally averaged intensity profiles, namely, $\overline{I}^*(z_f,\ t) = 0.85$. The front trajectory of pressure experiments with the flushing stage (solid, colored lines) and without the flushing stage (dashed, colored lines) are shown. The black dotted lines show the best fit of Eq. (8) after the onset of convection. Note that the position of the front $z_1 = z_f(t_1)$, and the time at the onset of convection t_1 have been subtracted from $z_f(t)$ and t, respectively.

C. Onset of convection

We start our analysis of the short-time, transient behavior by looking at the onset of convection and the influence of the cylinder widths and CO_2 pressure inside the tank. As shown in our previous work, [32], at the onset of convection, the Rayleigh number of the system has become equal to the critical Rayleigh number, based on the thickness $\delta(t)$ of the boundary layer

$$\mathrm{Ra}_\delta \equiv \frac{\beta k_H P_{\mathrm{CO}_2} g \delta^3}{\nu D}, \tag{5}$$

where $\beta = 8.2 \times 10^{-6}$ m^3/mol is the solutal expansion coefficient of CO_2, $k_H = 3.53 \times 10^{-4}$ mol/m^{3}Pa the Henry constant of CO_2 in water, P_{CO_2} the partial pressure of CO_2 inside the experimental chamber, g the acceleration due to gravity, $\nu = 9.5 \times 10^{-7}$ m^2/s the kinematic viscosity of water, and $D = 1.85 \times 10^{-9}$ m^2/s the diffusion coefficient of CO_2 in water [7,34,39,40].

Taking the boundary layer thickness equal to the position of the front at the time we observe the onset of convection, i.e., $\delta = z_f(t_1) = z_1$ obtained from Figs. 3 and 5, we obtain the corresponding critical Rayleigh numbers. Furthermore, we define the local aspect ratio based on the position of the front, $\Gamma = d/z_1$, where d is the diameter of the cylinder used. That is, this is the aspect ratio of the region of the cylinder that has been affected by the diffusion of the CO_2 at the moment convection sets in. As a result, we obtain Fig. 6, where the average critical Rayleigh number (red/blue markers) as a function of the aspect ratio at the onset of convection for the different cylinder widths and partial CO_2 pressures is shown. The error bars show the standard deviation of the average critical Rayleigh numbers, indicating the spread of the individual experiments (gray markers). It should be noted that the individual experiments are organized on diagonal lines in this doubly logarithmic plot, which is due to both Ra_c and Γ being dependent on the boundary layer thickness.

We compare our findings to the expression given by Ahlers *et al.* for the critical Rayleigh number for Rayleigh-Bénard convection in a cylinder [34]:

$$\mathrm{Ra}_c \equiv 1708\left(1 + \frac{C}{\Gamma^2}\right)^2. \tag{6}$$

Fitting Eq. (6) to the individual experiments shown in Fig. 6 results in finding $C = 1.413$ (gray dotted line), while fitting only the averages of the experiments results in finding $C = 1.335$ (dashed black line). In their work, Ahlers *et al.* provide the theoretical C for isothermal sidewalls, $C = 1.49$ (solid black line), which Fig. 6 shows to result in a very good agreement between Eq. (6) and

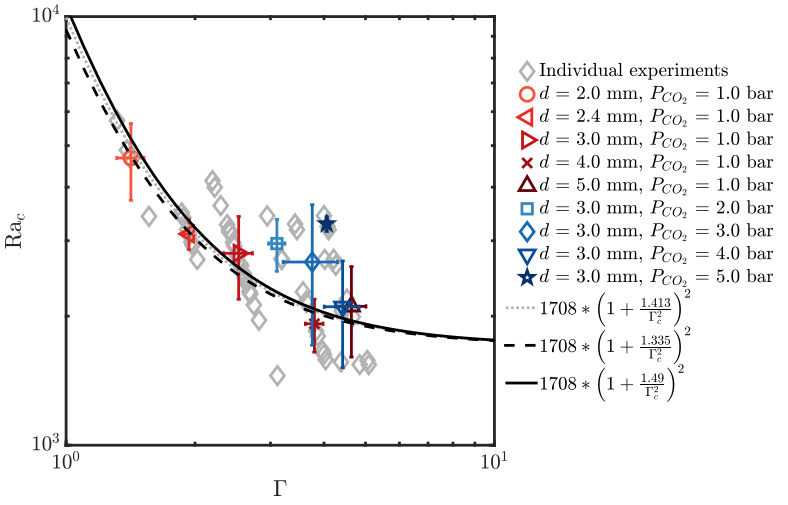

FIG. 6. Average critical Rayleigh number Ra_c (red/blue markers) as a function of the aspect ratio Γ at the onset of convection for different cylinder widths and partial CO_2 pressures. The error bars indicate the standard deviation of the calculated average due to spread in the individual experiments (gray diamonds). The lines show $\mathrm{Ra}_{c,\Gamma} = 1708(1 + C/\Gamma^2)^2$, with a best-fit C for both the individual experiments (dotted gray line), the averages (dashed black line), together with the theoretically predicted value of C for isothermal sidewalls (solid black line) from Ahlers *et al.* [34].

our experimental data. This is remarkable as the for our system more appropriate theoretical value for C for adiabatic sidewalls ($C = 0.77$) does not agree with our data. This is mostly likely due to differences between our mass transfer system and the Rayleigh-Bénard system, in depth described in Ref. [32]: Most prominently, we conduct our experiments at a higher Schmidt number, $\mathrm{Sc} = \nu/D = 515$, which needs to be compared to the corresponding, much smaller Prandtl numbers considered in Rayleigh-Bénard studies, $\mathrm{Pr} = 1$–10.

Nonetheless, two outliers can be observed in Fig. 6, corresponding to the $P_{\mathrm{CO}_2} = 3.0$ and 5.0 bar experiments respectively for a cylinder diameter of $d = 3.0$ mm. These are due to the difficulty in defining the point in time at which convection sets in for experiments conducted at partial CO_2 pressures above 3.0 bar. This resulted in a small overestimation of the onset time and thus the onset depth and given that the front depth z_1 is cubed in Eq. (5), results in the overestimation of Ra_c, visible in Fig 6.

D. Effective diffusion coefficients

We continue by studying the coupling between the density-driven convection and diffusion, resulting in the observed increased effective diffusion coefficients. Such an interplay between diffusion and convection in a confined environment, such as our narrow cylinder, leading to the enhanced dispersion of a solute in a solvent has been studied in literature for forced convective systems and is usually referred to as Taylor-Aris dispersion. Taylor and Aris independently developed a theoretical framework which links the effective diffusion coefficient of such a system to the underlying flow field:

$$D_{\mathrm{eff}} = D + \frac{U_f^2 r^2}{C_{TA} D} = D\left(1 + \frac{\mathrm{Pe}^2}{C_{TA}}\right), \tag{7}$$

where U_f is the velocity of the underlying flow field, r is the radius of the cylinder, C_{TA} is a constant dependent on the geometry of the system ($C_{TA} = 48$ for the fully developed pipe-flow system originally studied by Taylor and Aris), and the Péclet number is defined as $\mathrm{Pe} = rU_f/D$ [41–43].

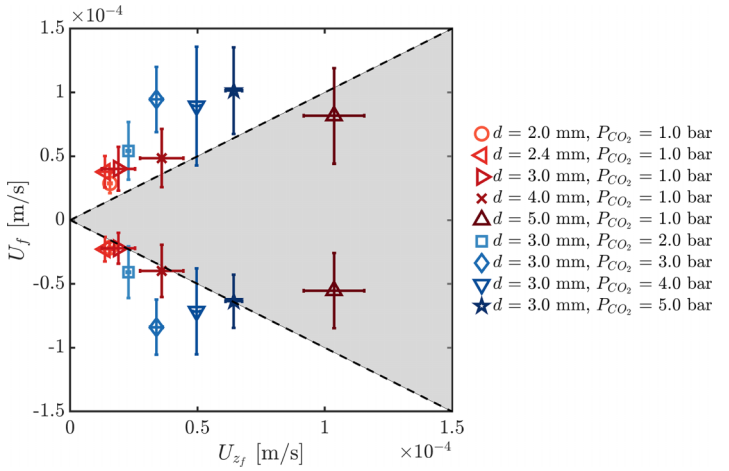

FIG. 7. Average flow velocity U_f as a function of the average CO_2 front velocity $\mathrm{d}z_f/\mathrm{d}t$. The positive flow velocities correspond to downward movement, and negative values to upward movement. The black dotted lines indicate $|U_f| = dz_f/\mathrm{d}t$, and the gray region indicates the area where $|U_f| < dz_f/\mathrm{d}t$.

In order to use Eq. (7) for our natural convective system, we first need to obtain the velocity of the underlying flow field as a function of cylinder width and CO_2 pressure. To that end, we performed 2D particle-tracking velocimetry experiments, following the procedure described earlier. Tracking the particles trapped in the recirculating flow field behind the CO_2 front allowed us to obtain the flow velocities needed. Note that, in the axisymmetric situation, U_f is dependent on both the radial coordinate r as well as the axial coordinate z and in a nonaxisymmetric breaking of the symmetry also on the third coordinate. In order to account for this, given that we are only able to track the particle in a 2D projection, we determined the velocities of a large number of particles and took the average of all velocities obtained for a given cylinder width and CO_2 pressure.

In Fig. 7 the obtained average flow velocities are compared to the average CO_2 front velocity, $\mathrm{d}z_f/\mathrm{d}t$, after the onset of convection. The positive flow velocities correspond to particles moving downwards in the cylinder, i.e., moving from the open interface at the top to the closed bottom, and consequently the negative flow velocities correspond to particles moving upwards. From the figure it is clear that particles, for the same inner diameter or partial pressure, move slightly faster in the downward direction compared to the upward direction. This can be traced back to the gravitational force acting upon the particle, which increases the particles velocity when moving towards the bottom and slowing down the particles movement when the particle is rising. Note that, although we use particles that are considered to be neutrally buoyant, the velocities that we are aiming to measure are such that also small density mismatches will have an effect.

We also observe that, for all cases studied except one, the average flow velocity is approximately equal to the average front velocity, $|U_f| \approx \mathrm{d}z_f/\mathrm{d}t$. This is expected given that the propagation of the CO_2 front is reliant on a steady supply of CO_2 in order to maintain the concentration gradients across the interface. If $|U_f| < \mathrm{d}z_f/\mathrm{d}t$, the concentration gradients at the front would slowly decrease and result in the front propagation stagnating, while the opposite, $|U_f| > \mathrm{d}z_f/\mathrm{d}t$, would result in a build up of CO_2 rich liquid at the front, possible leading to a secondary shedding event which has not been observed experimentally. Figure 7 does, however, show one case in which we find $|U_f| < dz_f/\mathrm{d}t$, which corresponds to the experiments in the cylinder with an inner diameter of $d = 5.0$. mm. This finding could be connected to the front never stabilizing and thus the front reaching the bottom of the cylinder before the entire width of the cylinder contains CO_2 rich liquid. Alternatively, it could be due to a larger influence of the 3D character of the flow field, e.g., due to multiple convection rolls being present in the system simultaneously.

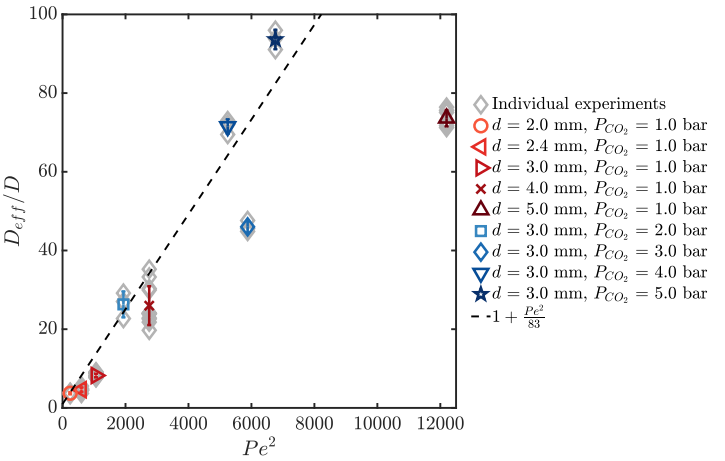

FIG. 8. Effective diffusion coefficients D_{eff}, rescaled with the diffusion coefficient D of CO_2 in water, as a function the squared Péclet number Pe for all experiments. The gray markers indicate individual experiments, and the red and blue markers indicate the average of the different experiments. The black dotted line shows $D_{\text{eff}}/D = 1 + \frac{Pe^2}{83}$.

Using the flow velocities obtained from the PTV experiments, we can calculate the Péclet number for the different experiments. We obtain the effective diffusion coefficients from Figs. 3 and 5 by fitting the front trajectories after the onset of convection using

$$z_f - z_1 = K_f \sqrt{D_{\text{eff}}(t - t_1)}. \tag{8}$$

For the pressure experiments, the average diffusion coefficient is calculated using both the flush and no-flush experiments, as flushing was shown not to affect the propagation dynamics after the onset of convection. The resulting average fits are shown as the black dotted lines in Figs. 3 and 5.

Finally, we show in Fig. 8 the effective diffusion coefficients obtained as a function of the Péclet number. Fitting the obtained data using Eq. (7), while excluding the outliers at $\text{Pe}^2 = 6200$ and $\text{Pe}^2 = 12500$, we find $C_{TA} = 83$. The excluded outlier at $\text{Pe}^2 = 6200$ is the experiment conducted at a pressure of $P_{\text{CO}_2} = 3$ bar, and it is due to measuring a flow velocity which is higher than expected, which can also be observed in Fig. 7. The second excluded outlier is the experiment with inner diameter $d = 5.0$ mm, as we do not believe that the measured effective diffusion coefficient reflects the necessary conditions needed to apply the Taylor-Aris dispersion theory, given that the front reaches the bottom interface before an axisymmetric front has been established. Furthermore we find $|U_f| < dz_f/\mathrm{d}t$ for this experiment, suggesting that the front propagates faster than the underlying flow velocity, which is physically impossible.

The obtained $C_{TA} = 83$ is higher compared to the value found by Taylor and Aris, who found $C_{TA} = 48$ for their system, but in the same ranges as reported by others for natural convective laminar flow in a vertical channel ($C_{TA} = 52.5$) and density-driven CO_2 convection in a Hele-Shaw cell ($C_{TA} = 210$) [41–45]. While our system is very comparable to the system studies by Taylor and Aris, some key differences lead us to find a higher C_{TA}. First of all and most importantly, Taylor and Aris studied a system in which the flow profile inside the cylinder has a parabolic profile, i.e., a Poiseuille flow, while the flow profile in our system is characteristic for a recirculating flow. Furthermore, our system is not in a steady state and the flow is still time dependent, while the flow in the system of Taylor and Aris is a steady, time-independent flow. Additionally, they described a horizontally aligned system, which results in gravity not affecting the propagation of the solute. Taylor did discuss the influence of gravity in a vertical aligned system in a later work, but did not

provide a value for C_{TA} [46]. Finally, the supply of solute for both Taylor's and Aris' case is limited, while we have a constant supply of CO_2 at the top interface. We therefore believe our $C_{TA} = 83$ to be very reasonable and usable to predict the effective diffusion coefficient of CO_2 in water in such a narrow, vertical cylinder.

In Apppendix A we will present a simplified convection model describing the time evolution of the convective flow $\bar{u}$ in the capillary, based on the (convective) CO_2 uptake at the water-CO_2-atmosphere interface, from which we conclude that $\bar{u}$ rapidly (after 100 seconds) converges to a steady state in which we argue that a Taylor-Aris dispersion approach consistutes the appropriate framework to discuss the motion of the CO_2-concentration front in our setup, thereby justifying the approach taken in this subsection.

IV. LONG-TIME, STEADY MASS TRANSFER DYNAMICS OF CO_2 IN THE LIQUID BARRIER

A. Influence of the barrier height

Thus far we have focused on the short-time, transient diffusion of CO_2 into the liquid barrier. We will now turn to the long-time, steady mass transfer dynamics in the liquid barrier, by trapping a slug bubble at the bottom of the cylinder, underneath the liquid barrier. Once the CO_2 front reaches the liquid-bubble interface, quasisteady convective transport develops in the barrier and the bubble starts to grow due to CO_2 exsolving from the liquid into the bubble. Therefore, we begin by analyzing a series of bubble growth experiments with bubbles of an starting volume of $V_f = 30$ µl, capped by a water layer with a thickness ranging between $H_w = 4.2$ mm and 28 mm. The CO_2 pressure inside the tank varies between $P_{CO_2} = 0.5$ bar to 4.0 bar. Figure 9 shows snapshots of typical bubble growth experiments. Cases (ix) and (x) show results for barrier heights $H_w = 4.2$ mm at $P_{CO_2} = 1.0$ and $P_{CO_2} = 3.0$ bar, respectively, while cases (xi) and (xii) show results for $H_w = 19.8$ mm at $P_{CO_2} = 1.0$ and $P_{CO_2} = 3.0$ bar. As expected, the slug bubble grows faster if the water barrier is smaller or the CO_2 pressure inside the tank is larger. We also observe that the liquid-gas meniscii in the early stages are non-axisymmetric. This is most likely due to the meniscii getting pinned on one side of the wall, while the other side remains unpinned and thus able to rise as the bubble grows.

We quantify these differences by plotting the increase in bubble volume with time, $\Delta V_b(t) = V_b(t) - V_f$, in Fig. 10(a) for barrier heights $H_w = 4.2$ mm, 12.7 mm, 19.8 mm, and 28 mm at CO_2 pressures of $P_{CO_2} = 1.0$ bar and 3.0 bar. The first observation that stands out is the aforementioned difference in bubble growth rates between the experiments, with decreasing bubble growth rate as the barrier height increases. Furthermore, we see that, for the same barrier height, the bubble growth rate increases as the CO_2 pressure is increased.

Figure 10(a) also shows that the bubble starts to grow at different time intervals after the start of the experiments. For example, at a CO_2 pressure $P_{CO_2} = 1.0$ bar, the bubble starts to grow around $t_{start} = 400$ s into the experiments for the barrier of height $H_w = 4.2$ mm, while it starts to grow at around $t_{start} = 2000$ s for $H_w = 28$ mm. The same is true for the experiments at higher pressure ($P_{CO_2} = 3.0$ bar); however, the starting times are decreased to $t_{start} = 60$ s for $H_w = 4.2$ mm and $t_{start} = 400$ seconds for $H_w = 28$ mm.

We quantify this behavior in Fig. 10(b), where the starting time t_{start} of the bubble growth is shown as a function of the barrier height H_w. The dotted lines act as visual guides and further underline the increase of the starting time of the bubble growth as the barrier height increases, of course due to the increased distance over which the CO_2 has to be transported before reaching the bottom liquid-gas interface. Furthermore, the influence of the CO_2 pressure on the start of the bubble growth is clear, indicating that higher CO_2 pressures result in earlier bubble growth. This is in agreement with our findings from Figs. 4 and 5, where we observed that the CO_2 front propagates faster at higher CO_2 pressures and thus reaches the liquid-bubble interface sooner. Finally, for $P_{CO_2} = 0.5$ bar and 1.0 bar points can be seen for which the bubble starts to grow much sooner than expected. This is due to the occurrence of the shedding of the upwelling plume,

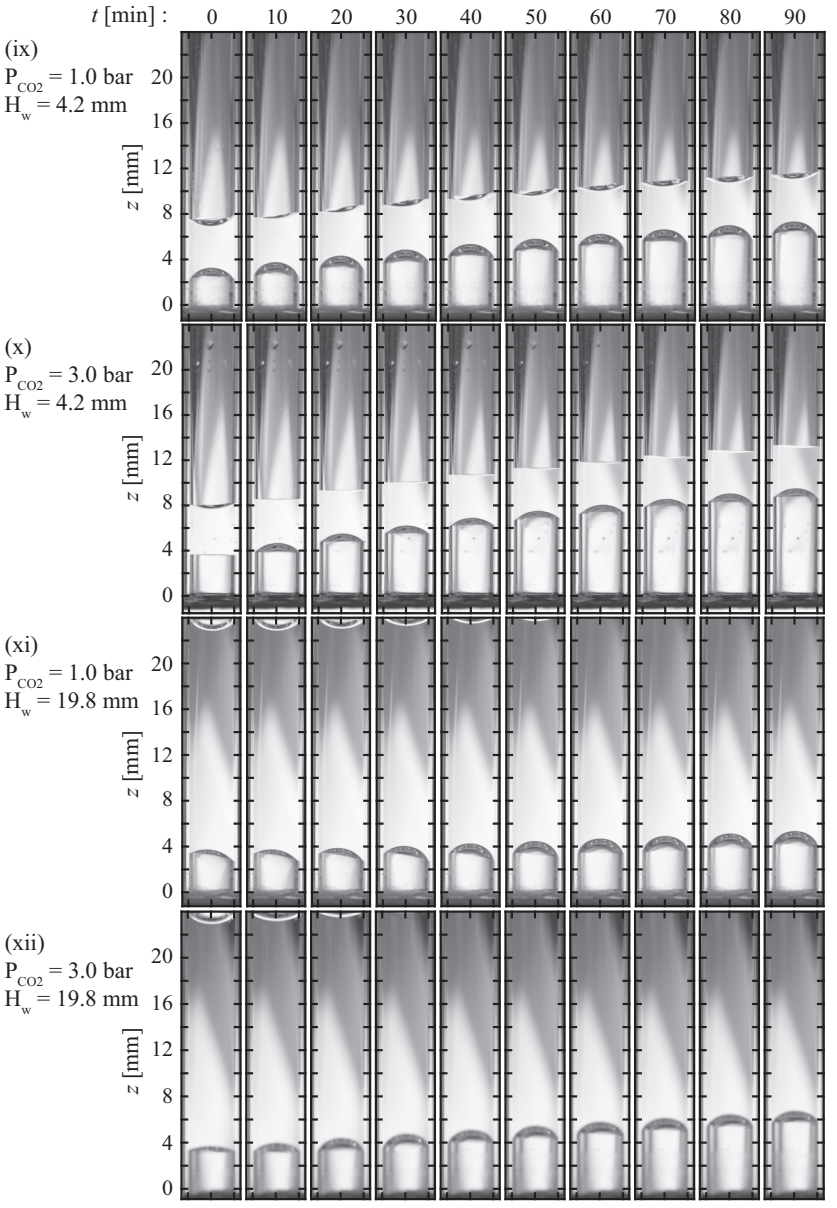

FIG. 9. Snapshots of typical slug bubble growth experiments within a cylindrical cell of inner diameter $d = 3.0$ mm. In (ix) the CO_2 pressure is $P_{CO_2} = 1.0$ bar and the barrier height is $H_w = 4.2$ mm, for (x) $P_{CO_2} = 3.0$ bar and $H_w = 4.2$ mm, for (xi) $P_{CO_2} = 1.0$ bar and $H_w = 19.8$ mm, and for (xii) $P_{CO_2} = 3.0$ bar and $H_w = 19.8$ mm.

which we observed earlier in Fig. 2 in experiment (ii). As explained previously, the upwelling plume causes the CO_2 front to accelerate to a higher velocity, leading to the front reaching the bottom interface faster in comparison to experiments in which the shedding of the upwelling plume does not occur [32]. As a result, the mass transfer between liquid barrier and the trapped bubble starts earlier, hence why we find these points at which the bubble starts growing earlier than expected.

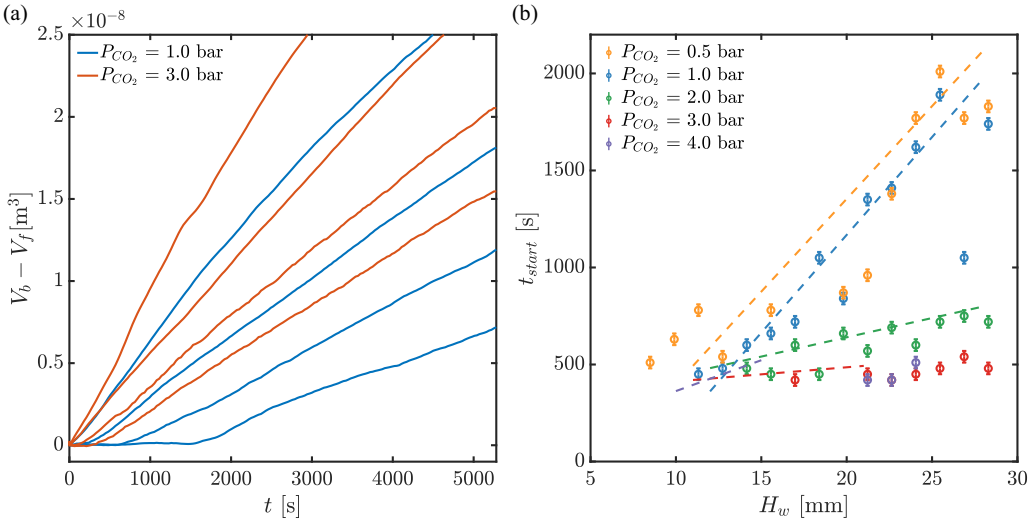

FIG. 10. (a) Time evolution of the bubble volume V_b minus the initial bubble volume v_f for increasing barrier heights H_w at $P_{CO_2} = 1.0$ bar (blue) and $P_{CO_2} = 3.0$ bar (red). (b) Time t_{start} at which the trapped slug bubble starts to grow as a function of the barrier height H_w. The dotted lines are included as visual guides.

B. Transport of CO_2 across the barrier

We characterize the convective transport of CO_2 across the water barrier using the Rayleigh and Sherwood numbers based on the evolution of the bubble volume in time and the bubble growth rate which we derived in earlier work [33]:

$$\mathrm{Ra}_w(t) = \mathrm{Ra}_f \frac{V_f}{V_b(t)}, \quad \text{where} \quad \mathrm{Ra}_f \equiv \frac{\beta k_H P_{\mathrm{CO}_2} g H_w^3}{\nu D} \tag{9}$$

and

$$\mathrm{Sh}_w(t) = \frac{\dot{V}_b(t)}{Q}\frac{V_b(t)}{V_f}, \quad \text{where} \quad Q \equiv D\frac{\pi d^2}{4H_w}(k_H R T_0). \tag{10}$$

Here $V_f = 30$ µl is the volume of the bubble after flushing and pressurisation, $V_b(t)$ is the volume of the bubble in time, $\dot{V}_b(t)$ is the bubble growth rate in time. Also recall that β is the solutal expansion coefficient of CO_2, k_H the Henry constant of CO_2 in water, P_{CO_2} the partial pressure of CO_2 inside the experimental chamber, g the acceleration due to gravity, H_w the height of the water barrier, ν the kinematic viscosity of water, D the diffusion coefficient of CO_2 in water, d the diameter of the cylinder, R the universal gas constant, and $T_0 = 295$ K the temperature inside the experimental chamber [7,39,40].

Figures 11(a) and 11(b) show the Rayleigh and Sherwood numbers, respectively, as a function of time calculated using Eqs. (9) and (10) for barrier heights of $H_w = 4.2$ mm, 17 mm, and 28 mm and CO_2 pressures of $P_{\mathrm{CO}_2} = 1.0$ bar and 3.0 bar. We observe that the Rayleigh number initially starts at $\mathrm{Ra}_w = \mathrm{Ra}_f$ and slowly decreases as volume of the bubble increases, however, it remains close to the starting value Ra_f. For the Sherwood number, we observe that, until the bubble starts to grow, it remains 0 after which it increases to an almost constant value at which point the growth rate of the bubble balances the decrease in concentration gradient between the outer atmosphere and the gas bubble. The rate at which the Sherwood number reaches its constant value is of course dependent on the barrier height and partial CO_2 pressure, reaching the constant Sherwood faster for shorter barriers and higher pressures.

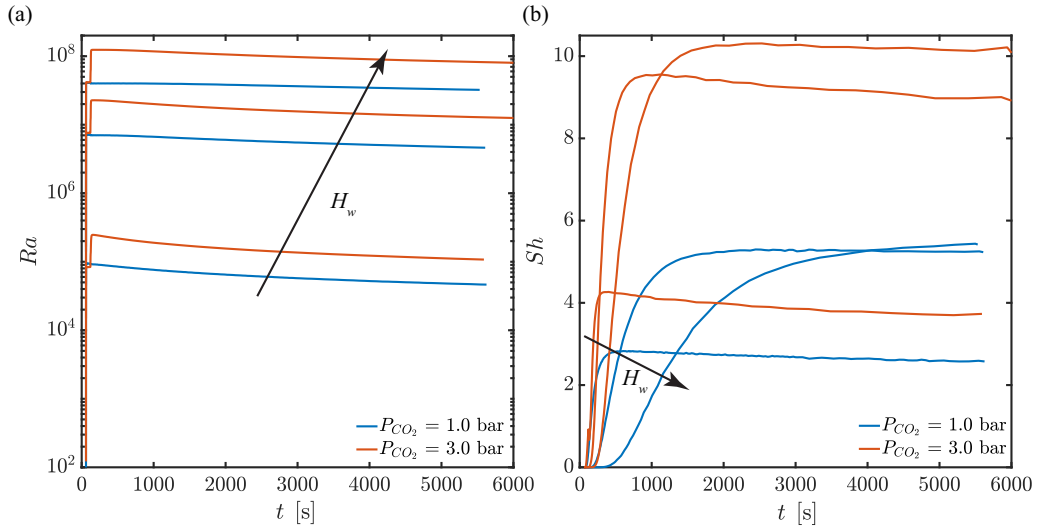

FIG. 11. (a) Evolution of the Rayleigh number Ra and (b) Sherwood number Sh for increasing barrier height $H_w = 4.2$, 17, and 28 mm at $P_{CO_2} = 1.0$ bar (blue) and $P_{CO_2} = 3.0$ bar (red), determined using Eqs. (9) and (10).

Evaluating Eqs. (9) and (10) results in Fig. 12(a), where the time-averaged Sh_w is plotted against the time-averaged Ra_w. Each marker represents an individual experiment, with larger barrier heights H_w corresponding to larger average Ra_w. All experiments were performed for the same inner diameter $d = 3$ mm. The time-averages are computed over the last 3000 s of each experiment, to discard the period during which the Sherwood number is not yet at its terminal value. The vertical and horizontal error bars indicate the range over which Sh_w and Ra_w, respectively, decay during that particular experiment. The black dotted line and surrounding green shaded region provide the $\mathrm{Sh}_w(\mathrm{Ra}_w)$ dependence in $\mathrm{Sh}_w = (1 + k\mathrm{Ra}_w/1708)^{1/4}$, with $k = 2.75 \pm 1.25$, which we obtained in earlier work for the smaller liquid barriers and which is in agreement with the Grossman-Lohse theory for Rayleigh-Bénard convection [33,47–49].

Figure 12(a) does, however, clearly show that for each experimental series increasing the barrier height H_w the Sherwood number eventually reaches a maximum value, while the Rayleigh number continues to increase. This indicates that at some point the height of the liquid barrier is no longer the correct relevant length scale to be used in Eq. (9). This makes sense as the Sherwood number has a clear upper limit because the transport through the barrier saturates above some barrier height, since adding additional height is not increasing the (convective) CO_2 transport through the liquid barrier because its width is now the limiting factor. This effect can be incorporated by redefining the Rayleigh number based upon this aspect-ratio-dependent length scale.

In their work, Ahlers *et al.* provide such a relevant length scale for Rayleigh-Bénard convection [34],

$$l = H_w/\sqrt{1 + C/\Gamma^2} = H_w\sqrt{\frac{\Gamma^2}{C + \Gamma^2}}, \tag{11}$$

where C is a constant that depends on the shape of the cell, and is in fact the same constant as in Eq. (6). Note that Γ is now defined as $\Gamma = d/H_w$, based on the diameter d and the barrier height H_w, whereas previously it was defined with respect to the boundary layer thickness at the onset $\delta = z_{f,c}$. Inserting this length scale in the definition of the Rayleigh number leads to

$$\mathrm{Ra}_{w,l} = \frac{\beta k_H P_{\mathrm{CO}_2} g l^3}{\nu D} = \frac{\beta k_H P_{\mathrm{CO}_2} g H_w^3}{\nu D}\frac{l^3}{H_w^3} = \mathrm{Ra}_w\left(\frac{\Gamma^2}{\Gamma^2 + C}\right)^{3/2}. \tag{12}$$

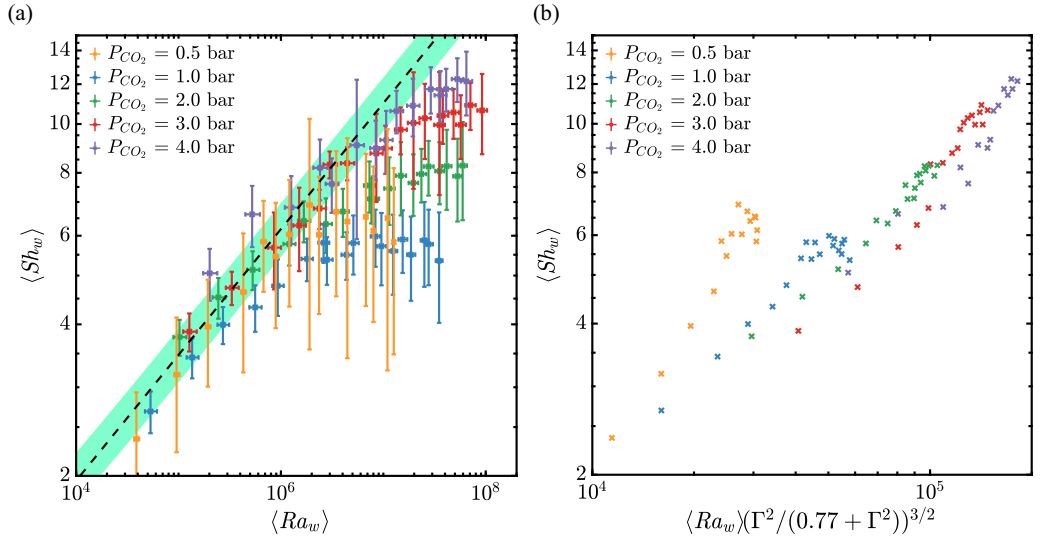

FIG. 12. (a) Time-averaged Sherwood number Sh_w as a function of the time-averaged Rayleigh number Ra_w for partial CO_2 pressures ranging from $P_{CO_2} = 0.5$ bar to 4.0 bar and barrier heights H_w ranging from 3.0 to 28.0 mm. The error bars indicate the range over which $\mathrm{Sh}_w(t)$ and $\mathrm{Ra}_w(t)$ decay during that particular experiment. Each marker represents an individual experiment, with larger barrier heights H_w corresponding to larger average Ra_w. All experiments were performed for the same inner diameter $d = 3$ mm. The black dotted line and surrounding green-shaded region provide the $\mathrm{Sh}_w(\mathrm{Ra}_w)$ dependence in $\mathrm{Sh}_w = (1 + k\mathrm{Ra}_w/1708)^{1/4}$, with $k = 2.75 \pm 1.25$ [33]. (b) Time-averaged Sh_w as a function of the rescaled, time-averaged Ra_w using the proper length scale l from Eq. (11) for partial CO_2 pressures, ranging from $P_{CO_2} = 0.5$ bar to 4.0 bar.

Rescaling the data from Fig. 12(a) using Eq. (12) results in Fig. 12(b), using $C = 0.77$, the best-fit constant for adiabatic sidewalls. We find very reasonable collapse of the data, where the correction most strongly affects the data for the larger values of H_w, with the only outliers being the data obtained of the $P_{CO_2} = 0.5$ bar experiments. This indicates that the partial CO_2 pressure inside the tank may not have been as close to 0.5 bar as expected, which is probably due to the method used to prepare the gas mixture. As explained in Sec. II, an equal amount of N_2 and CO_2 gas was injected into an external tank to obtain a 50% N_2 and 50% CO_2 gas mixture, which was subsequently injected into the measurement tank for the 0.5 bar experiments. However, we did not have the means to measure the partial CO_2 pressure in the measurement tank, so it could have been that the partial CO_2 pressure was in fact smaller than 0.5 bar. Furthermore, we see that the Rayleigh number no longer increases once the Sherwood number stabilizes, indicating that Eq. (11) indeed provides a proper rescaling of the relevant length scale for our experiments. The fact that we now obtain a good fit for $C = 0.77$, while for the onset of convection we found $C = 1.49$ to be the best fitting value, can possibly be explained by the differences in the systems studied. When looking at the onset of convection, our system is clearly not in a steady state, with a growing diffusive layer and therefore changing aspect ratio while in the current experiments our system has in fact reached a quasi steady state, such that the latter is expected to be more similar to the Rayleigh-Bénard systems studied in Ref. [34].

V. CONCLUSIONS

We have investigated dissolution and subsequent propagating dynamics of carbon dioxide gas into liquid barriers of varying height confined to a vertical glass cylinder of varying inner diameter under atmospheric and increased gas pressures. This allows us to study the influence of confinement

on the CO_2 transport into a narrow liquid barrier. Replacing the ambient air above the cylinder with a CO_2 atmosphere, induces the dissolution of CO_2 into the liquid barrier. Initially, the dissolution of CO_2 results in the formation of a CO_2-rich water layer, which is denser in comparison to pure water, at the top gas-liquid interface. While initially stable, continued dissolution of CO_2 into the water barrier results in the layer becoming gravitationally unstable, leading to the onset of buoyancy-driven convection and, consequently, the shedding of a buoyant plume. By adding sodium fluorescein, a pH-sensitive fluorophore, we directly visualize the dissolution and propagation of the CO_2 across the liquid barrier.

First, we studied the short-time, transient diffusion of CO_2 into the liquid barrier by looking at the onset of convention and its dependence on the cylinder diameter and CO_2 pressure by calculating the critical Rayleigh number at the onset of convection. We find that the critical Rayleigh number of our system can be described by the theory developed for critical Rayleigh number in Rayleigh-Bénard convection based on the aspect ratio of the cylinder width and corresponding front propagation depth. Second, by combining the fluorescence experiments with particle-tracking velocimetry measurements, we were able to extract the underlying flow velocities which allows us to study the coupling between density-driven convection and diffusion. Utilizing the framework of Taylor-Aris dispersion, we find an expression which gives the dependence of the effective diffusion coefficient after the onset of convection as a function of the Péclet number. Finally, we turned from transient to fully developed mass transfer across the liquid barrier by quantifying the growth of a slug bubble, trapped below the barrier using the Sherwood and Rayleigh numbers. We showed that initially the Sherwood number scales to the 1/4 power of the Rayleigh number, but for sufficiently large barrier heights stagnates, which we correct by rescaling the Rayleigh number with an aspect-ratio-dependent relevant length scale.

Our findings may be useful for laterally confined CO_2 sequestration operations, e.g., those where CO_2 diffuses from above into a porous medium. Such a medium can be viewed as a collection of small, vertical channels into which the CO_2 diffuses and in which the occurrence of convection may greatly enhance mass transport into the porous structure. In addition, they may offer insight in microfluidic or microreactor devices, which include (vertically) segmented gas-liquid systems or density-changing solutes. Here confined buoyancy-driven convection rolls similar to the ones observed and studied in our idealized system may very well occur. A better understanding of the dependence of the formation and propagation dynamics of the convective plume on the geometry and parameters of the system, may well uncover or explain unexpected mechanics that occur during the dissolution or mixing of chemical species in a variety of applications similar to the ones mentioned above.

ACKNOWLEDGMENTS

We wish to thank Vincent Bertin, Dominik Krug, Pablo Peñas-López, and Farzan Sepahi for very insightful discussions. This work was supported by the Netherlands Center for Multiscale Catalytic Energy Conversion (MCEC), an NWO Gravitation programme funded by the Ministry of Education, Culture and Science of the government of the Netherlands.

APPENDIX: CONVECTIVE INSTABILITY IN A CAPILLARY

In this Appendix we will discuss a simplified model for the convective transport in a narrow capillary tube. First, we will discuss a simple mechanism for the onset of convective motion in a capillary, which subsequently leads to an equation of motion in Appendix A 1. Since in the confined system a purely convective transport of the cross-sectionally averaged CO_2-concentration front is prohibited due to mass conservation, in Appendix A 2 we subsequently discuss how the concentration front diffusively propagates, in the context of Taylor-Aris diffusion.

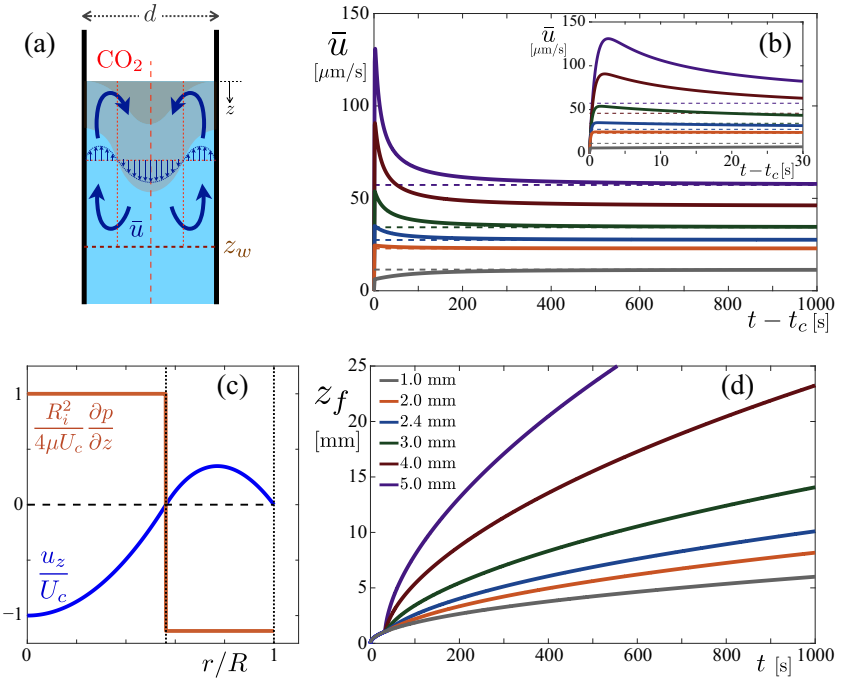

FIG. 13. (a) Sketch of an axisymmetric convective flow of magnitude $\bar{u}$ inside a cylindrical capillary of diameter d, confined by the cylinder walls, the free surface, and some depth $z_w(t)$. The darker areas denote CO_2-rich water, which upon convection onset at the critical Rayleigh number drives the convective flow by moving down in the center of the capillary. Note that $z = 0$ at the free surface (which for the purpose of the model is assumed flat) and z increases with increasing depth. (b) Time evolution of the convective velocity magnitude $\bar{u}$, computed from the model of Eq. (A8) for capillaries of different width ($d = 1.0, 2.0, 2.4, 3.0, 4.0, 5.0$ mm) corresponding to those of the experiments of Fig. 3. The unknown numerical parameters $a_w = 2.5$, $a_v = 2.0$, and $a_z = 0.85$ have been chosen such that the asymptotic values $\bar{u}_{st}$ of Eq. (A15) are comparable to the measured velocities reported in Fig. 7. The inset shows the same data zooming in at the first 30 s. (c) Axisymmetric flow field $u_z(r)$ nondimensionalized with the central velocity magnitude U_c from Eq. (A18) and the vertical pressure gradient $\partial p/\partial z$, rescaled with $4\mu U_c/R_i^2$, both plotted as a function of the normalized radial coordinate r/R. The vertical dotted lines indicate the location of the inner-outer region boundary at $r/R = R_i/R = x$, and the cylinder wall at $r/R = 1$. (d) Time evolution of the diffusive front z_f for the data plotted in (b) computed by inserting the time-dependent Péclet number $\mathrm{Pe}(t) = \bar{u}(t)d/(2D)$ into the Taylor-Aris formula Eq. (7) to obtain a (time-dependent) effective diffusion coefficient which is subsequently used in Eq. (8) to compute $z_f(t)$. Note that in the Taylor-Aris formula $C_{TA} = 120$ was used, consistent with the diameter data in Fig. 8.

1. A simplified convection model

Before we start with the ingredients of the model, we first note that our capillary system is in the viscous limit. This can be corroborated by computing the Reynolds number Re based on the experimentally measured convective velocity as reported in Fig. 7, which leads to values between $\mathrm{Re} = 0.01$ and 0.5 for the smallest and the largest diameter, respectively. Now, assuming that after onset of convection a (time-dependent) liquid mass $M_w(t)$ of vertical extent $z_w(t)$ is set into motion [see Fig. 13(a)] and assuming that $\bar{u}(t)$ is the magnitude of the (vertical) convective flow velocity in this domain, we may write an equation of motion by equating the vertical momentum change inside the domain with the sum of the forces acting in the vertical direction

$$\frac{d}{dt}(M_w\bar{u}) = F_z - F_v\,, \tag{A1}$$

where F_z is the buoyancy force caused by the inflow of CO_2 into the domain, which is driving the convective flow, and F_v is the viscous force that opposes the flow. More specifically, one may split the buoyancy force term into two contributions, namely the mass increase m_w^* that has been caused by the diffusive transport of CO_2 into the capillary at the moment that the layer becomes unstable, which is a constant determined by the critical Rayleigh number Ra_c, and the mass increase $\Delta m_w^*(t)$ caused by uptake of CO_2 by the system after convection has set in, which obviously will depend on the magnitude of the convective flow $\bar{u}$. Inserting the above two quantities into Eq. (A1) gives

$$\frac{d}{dt}[M_w(t)\bar{u}(t)] = m_w^* g + \Delta m_w^*(t) g - F_v(t). \tag{A2}$$

We will now provide estimates for the four terms in the equation. This requires us to dive a bit deeper into the structure of the flow, which for the sake of definiteness we will assume to be axisymmetric as sketched in Fig. 13(a). First of all, buoyancy is driving the flow in a region that is confined by the cylinder walls, the free surface, and some depth $z_w(t)$ which remains to be determined. The flowing mass M_w can thus be written as $M_w(t) = \frac{1}{4}\pi d^2 z_w(t)\rho_w$, where d is the diameter of the capillary and ρ_w the density of water (neglecting the small overall increase of the density caused by the uptake of CO_2 for this term).

The first term on the left hand side is determined by the amount of CO_2 that has diffused into the water in the capillary. Neglecting the curved shape of the meniscus, the time t_c at which the CO_2 layer becomes unstable can be found by inserting the critical layer thickness $\delta_c = K_f\sqrt{Dt_c}$ [from Eq. (3)] in the critical Rayleigh number $\mathrm{Ra}_\delta(t) = \beta C_{\mathrm{sat}} g \delta(t)^3/(\nu D) = \mathrm{Ra}_c$, with $C_{\mathrm{sat}} = k_H P_{\mathrm{CO_2}}$. Here, for notational simplicity, we assumed that $t = 0$ corresponds to the time the interface is first exposed to the CO_2 atmosphere. This leads to $t_c = K_f^{-2} D^{-1/3}[\nu \mathrm{Ra}_c/(\beta C_{\mathrm{sat}} g)]^{2/3}$. From Eq. (2) we can compute the diffusive flux q'' through the free surface

$$q''_{z=0} = -D\left.\frac{\partial C(z,t)}{\partial z}\right|_{z=0} = C_{\mathrm{sat}}\sqrt{\frac{D}{4\pi t}}\,. \tag{A3}$$

Multiplying the diffusive flux with the cross-sectional area of the capillary and integrating until t_c gives the mass $m^*_{CO_2}$ of CO_2 diffused into the water at convection onset

$$m^*_{CO_2} = \frac{1}{4}\pi d^2 \int_{t=0}^{t_c} q''_{z=0} = \frac{1}{4} d^2 C_{\mathrm{sat}}\sqrt{\pi D t_c}\,. \tag{A4}$$

Note that this is not yet the sought-after quantity m_w^* which is obtained by multiplying $m^*_{\mathrm{CO_2}}$ with $\beta\rho_w$, since it is the integrated surplus density of the liquid caused by the CO_2 uptake that drives the convection, and not the mass of CO_2 in the liquid itself. So finally we obtain

$$m_w^* = \beta\rho_w m^*_{\mathrm{CO_2}} = \frac{\sqrt{\pi}}{4}\frac{\beta\rho_w C_{\mathrm{sat}} d^2}{K_f}\left(\frac{\nu D \mathrm{Ra}_c}{\beta C_{\mathrm{sat}} g}\right)^{1/3}. \tag{A5}$$

It is good to note that in the above expression we have not corrected for finite aspect ratio of the affected part of the capillary, which may however unproblematically be included along the lines outlined in Sec. III.

Next we discuss the convective term $\Delta m_w^*(t)$ in Eq. (A2). As soon as the convective flow of magnitude $\bar{u}$ has set in, fresh liquid will be brought in from the capillary walls to the free surface and flow towards the center, where the growing diffusive boundary layer will have reached a thickness $\delta_{in} \sim \sqrt{Dd/(2\bar{u})}$ [50]. Since the speed of entrainment is $\bar{u}$, the mass flow of CO_2 into the water can be estimated as $q_{CO_2} \sim \delta_{in}\bar{u}C_{\mathrm{sat}}(d/2)$, where we have estimated the azimuthal lengthscale over which liquid is entrained as $d/2$. The surplus mass $\Delta m_w^*(t)$ added to the system can now be found by multiplying $q_{\mathrm{CO_2}}$ with $\beta\rho_w$ and integrating over time

$$\Delta m_w^*(t) = a_z \frac{\beta\rho_w C_{\mathrm{sat}} d^{3/2} D^{1/2}}{2\sqrt{2}} \int_{s=t_c}^{t} \sqrt{\bar{u}(s)}\, ds, \tag{A6}$$

where we have introduced a numerical prefactor a_z which is expected to be of order one.

Finally, the viscous drag F_v in Eq. (A2) can be estimated from the drag force on the inner cylinder outlined in Fig. 13(a), namely, $F_w \approx \mu_w(\partial u/\partial r)A_{cyl}$, where $\partial u/\partial r \sim \bar{u}/(d/4)$ and $\mu_w = \rho_w \nu$ and $A_{cyl} = 2\pi(d/4)z_w$ are the dynamic viscosity of water and the surface area of the inner cylinder, respectively. Noting that a drag of similar magnitude must act for the upward flow in the outer cylindrical shell, we may write

$$F_v = 4\pi a_v \mu_w z_w \bar{u}\,, \tag{A7}$$

where again we have introduced an order one numerical prefactor a_v.

Inserting the four terms into Eq. (A2) now leads to the following integral-differential equation for the unknown parameters $\bar{u}$ and z_w:

$$\frac{d}{dt}(z_w\bar{u}) \;= \Gamma + \Lambda \int_{s=t_c}^{t} \sqrt{\bar{u}(s)}\, ds \;-\; \frac{z_w\bar{u}}{\tau_v}, \tag{A8}$$

where we have defined the quantities

$$\Gamma = \frac{4m_w^* g}{\pi d^2 \rho_w}, \quad \Lambda = \frac{2a_z}{\pi\sqrt{2}} \frac{\beta C_{\text{sat}} D^{1/2} g}{d^{1/2}}, \quad \tau_v = \frac{d^2}{16 a_v \nu}, \tag{A9}$$

where τ_v is a viscous time scale, Γ has the dimensions of a squared velocity and the unit of Λ is $\mathrm{m}^{3/2}\,\mathrm{s}^{-5/2}$.

The time evolution of the CO_2 concentration in the capillary starts with a first, diffusive stage, which lasts until the convection onset time t_c. At this moment, the CO_2-rich layer at the top of the capillary starts to become unstable and a convective flow sets in. At first, this convective flow is not yet balanced by viscous forces, and an initial large acceleration occurs. This is the second or inertial stage. It may be analyzed from Eq. (A8) by neglecting the second term on the right hand side that accounts for the convective uptake of CO_2 at the free surface. Without that term, the resulting differential equation for the product $z_w\bar{u}$ is readily integrated from t_c onwards, with boundary condition $\bar{u}(t_c) = 0$, which leads to the solution

$$z_w\bar{u} = \Gamma\tau_v\left(1 - \exp\left[-\frac{t - t_c}{\tau_v}\right]\right), \tag{A10}$$

where it is good to note that for the parameter range studied in this article the viscous timescale is of the order of a few tenths of seconds ($\tau_v \approx 0.1$–1.5 s for $a_v = 1$).

Now, clearly, the above approximation allows us to obtain the time evolution of the product $z_w\bar{u}$, but not that of z_w and $\bar{u}$ separately, which needs additional approximations. Now, from a physical perspective, it makes sense that speed with which the region that is affected by the convective motion grows is directly proportional to the convective flow strength, that is,

$$\frac{dz_w}{dt} = \frac{1}{2} a_w \bar{u}, \tag{A11}$$

where a_w is again a numerical prefactor of order unity. Inserting the above assumption into Eq. (A10) allows us to integrate a second time

$$z_w(t) = \sqrt{z_w(t_c)^2 + a_w\Gamma\tau_v\left[(t - t_c) + \tau_v\left(\exp\left[-\frac{t - t_c}{\tau_v}\right] - 1\right)\right]}, \tag{A12}$$

where the boundary condition $z_w(t_c)$ needs to be defined, but it appears reasonable to assume that it is something like twice the thickness of the marginally stable CO_2-rich layer, namely, $z_w(t_c) = 2\delta(t_c)$. For times much larger than t_c one may appreciate that z_w goes to infinity as $t^{1/2}$ and $\bar{u}$ to zero as $t^{-1/2}$ keeping the product constant $z_w\bar{u} \approx \Gamma\tau_v$. Clearly, this is due to neglecting the second term on the right-hand side of Eq. (A8), which accounts for the convective transport into the capillary.

It is straightforward but a bit tedious to use the long-time limit of the above solution to estimate when the second term on the right-hand side of the equation of motion (A12) becomes of the same

order as the first. The result is

$$t - t_c = \left[\frac{6\sqrt{2}}{a_z \pi}\right]^{4/3} \left[\frac{a_w}{\Gamma \tau_v}\right]^{1/3} \left[\frac{m_w^*}{\beta C_{\text{sat}} D^{1/2} d^{3/2} \rho_w}\right]^{4/3}, \tag{A13}$$

which leads to a timescale between 8 and 32 s for the parameter values used in the experiment, that is, about an order of magnitude larger than the viscous time τ_v.

Finally, one may numerically solve the pair of ordinary differential-integral equations (A8) and (A11), using boundary conditions $\bar{u}(t_c) = 0$ and $z_w(t_c) = 2\delta(t_c)$, the result of which is provided in Fig. 13(b) for the same parameter values as used in the experiment of Fig. 3. Clearly, the magnitude of the convective velocity goes to a constant value quite rapidly, which may easily be understood as a balance of the driving and the viscous force in Eq. (A1): $F_z = F_v$. Taking the time derivative of the right-hand side [51] of Eq. (A8) leads to

$$\Lambda \sqrt{\bar{u}} = \frac{1}{\tau_v}\left[\bar{u}\frac{dz_w}{dt} + z_w \frac{d\bar{u}}{dt}\right] \approx \frac{1}{\tau_v}\bar{u}\frac{dz_w}{dt}, \tag{A14}$$

where the last approximation is made in search of a steady state solution ($d\bar{u}/dt \approx 0$). Using Eq. (A11), this expression is readily solved for the steady state value $\bar{u}_{st}$ of $\bar{u}(t)$

$$\bar{u}_{st} = \left(\frac{2\Lambda \tau_v}{a_w}\right)^{2/3} = \left(\frac{a_z}{4\sqrt{2} a_v a_w}\right)^{2/3} \left(\frac{\beta C_{\text{sat}} g}{\nu}\right)^{2/3} D^{1/3} d\,. \tag{A15}$$

The values $\bar{u}_{st}$ are plotted as the horizontal dashed lines in Fig. 13(b) for the different capillary diameters and agree well with the asymptotic behavior of $\bar{u}(t)$.

2. Taylor-Aris diffusion

Now that we have formulated an equation of motion for the average convective velocity in the previous subsection, it is good to stress that, as a result of convection only, the average position of the front cannot move. For a cylinder that is closed at the bottom, any arbitrary surface S within the liquid intersecting the cylinder can be closed along the cylinder walls where the velocity is zero, such that, using Gauss' formula and incompressibility

$$\iint_S \vec{u} \cdot d\vec{S} = \iiint_V (\vec{\nabla} \cdot \vec{u})\, dV = 0, \tag{A16}$$

where V is the liquid volume in the cylinder below the intersecting surface S. If we now let S coincide with the position of the diffusive front at some arbitrary time t, then some time later the shape of this front may have been altered due to convective flow, as a result of some liquid streaming upward and some downward with respect to S, but because the net average flow through S must be zero, this can never lead to a downward (or upward) displacement of the front as a whole. So the front needs to vertically displace in a diffusive manner and the way in which convection may enhance this diffusion is by stretching and thereby steepening the diffusive front, as we already observed in a previous publication [32]. In this stretching process, the thickness of the front decreases which in turn increases its diffusive propagation speed.

Clearly, the front must be located somewhere in the central part of the convection roll and, as a result, the situation is similar to the one studied independently by Taylor [41] and Aris [42] for diffusion enhancement in a Poiseuille flow and later extended by many others [43,44,52–56] to more general types of flow, including also time-dependent pulsating flows. For an axisymmetric steady laminar flow $v(r)$ in a cylindrical pipe of radius R one may write that the enhanced diffusion can be described by an effective diffusion coefficient given by

$$D_{\text{eff}} = D + \frac{2}{DR^2} \int_{r=0}^{R} \left[\int_{s=0}^{r} (v(s) - \bar{v}) s\, ds\right]^2 \frac{dr}{r}, \tag{A17}$$

where $\bar{v}$ is the average velocity in the pipe. It is straightforward to show that for Poiseuille flow $v(r) = v_c(1 - (r/R)^2)$ the integration leads directly to Eq. (7) with $C_{TA} = 48$ if the Péclet number is defined with respect to the mean flow $\bar{v} = v_c/2$, i.e., $\mathrm{Pe} = \bar{v}R/D$.

However, in our case the flow inside the capillary is expected to depart in many aspects from a Poisseuille flow, and therefore we decided to construct a solution $u_z(r)$ of the axisymmetric Navier-Stokes equations that satisfies the following conditions: (i) the cylinder is split in an inner region of radius R_i with a constant upward pressure gradient $K_i = (\partial p/\partial z)_i$ (leading to a downward flow), and an outer region with a constant downward pressure gradient of different magnitude $K_o = -(\partial p/\partial z)_o$, (ii) $u_z(r)$ and its derivative are continuous in $r = R_i$, (iii) the net flow is zero, and (iv) there is no slip at the outer wall. These conditions are necessary and sufficient to fix the shape of the profile $u_z(r)$, the ratios $x = R_i/R \approx 0.5623$ and $y = K_o/K_i \approx 1.1386$, leading to [57]

$$\frac{u_z(r)}{U_c} = \begin{cases} -\left(1 - r^2/R_i^2\right) & \text{if } r \leqslant R_i \\ -y\left(r^2/R_i^2 - 1\right) + 2(y+1)\log(r/R_i) & \text{if } R_i < r \leqslant R \end{cases}, \tag{A18}$$

where $U_c = -u_z(0)$ is the magnitude of the central velocity. It should be stressed that, although the flow field (A18) is physical from the viewpoint of the above conditions, it has characteristics that are not consistent with the system studied, the most salient one being that for these parameters the upward forcing of the outer region is much larger than the downward forcing of the inner region, which could only be mended at the cost of one of the other conditions, such as continuity of the stress at the inner-outer region boundary, or by relaxing the simple form of the pressure gradient inside the cylinder. The only purpose of the above flow field however is to compute the Taylor-Aris constant C_{TA}, which may be done by rewriting the expression (A17) as $D_{\mathrm{eff}}D - D^2$ where the integral may be evaluated numerically leading to $D_{\mathrm{eff}}D - D^2 = 8.9696 \times 10^{-3}\, U_c^2 R^2$. To obtain C_{TA} one now needs to divide U^2R^2 by $D_{\mathrm{eff}}D - D^2$, where U is the velocity scale used to define the Péclet number. Clearly, depending of the choice for U one will obtain a different value for C_{TA}, ranging from $C_{TA} = 6$, 14, 26 to 111 where U is respectively the average upward velocity $\bar{u}_o = 0.23U_c$, the maximum upward velocity $U_{\max} = 0.35U_c$, the average downward velocity $|\bar{u}_i| = \frac{1}{2}U_c$, and the central velocity U_c. For the experiments discussed in Sec. III D, where the measured velocities are definitely closer to the largest velocities in the system than the average ones, finding a value of $c_{TA} \approx 84$ is therefore plausible.

In summary, the simplified model of Appendix A 1 predicts a convective velocity that after a short period of rapid change, consistent with the viscous time scale of several seconds, more slowly converges towards a steady state velocity. The slow change of the velocity after the first 100 s [cf. Fig. 13(b)] together with the observation that the position of the diffusive front must be central in the region affected by convective flow makes it plausible to use the Taylor-Aris formalism derived for steady axisymmetric flow in a pipe [Eq. (A17)] to determine an effective diffusion coefficient D_{eff}, which rationalizes the pseudo-diffusive behavior that we have observed after convection onset in the present and earlier work [32].

To finalize the arguments put forward in this Appendix, using the velocity $\bar{u}(t)$ obtained from the simplified model depicted in Fig. 13(b), we compute an effective diffusion coefficient $D_{\mathrm{eff}}(t)$ using the Taylor-Aris equation (7) with $\mathrm{Pe}(t) = \bar{u}(t)d/(2D)$, and subsequently insert this effective diffusion coefficient in

$$z_f(t) - z_c = K_f\sqrt{D_{\mathrm{eff}}(t)(t - t_0)}, \tag{A19}$$

to estimate the time evolution of the diffusive front $z_f(t)$ after convection onset at $t = t_c$, which is subsequently plotted in Fig. 13(d). To take into account that diffusion does not start at the moment of convection onset but had already been in progress, we (quite arbitrarily) set the initial time t_0 in this equation to the time at which the capillary was brought into contact with the CO_2 atmosphere, i.e., $t_0 = 0$. The curves plotted in Fig. 13(d) at least qualitatively resemble the corresponding experimental curves in Fig. 3, indicating that the simplified convection model together with the

thereby induced Taylor-Aris diffusion of the CO_2-concentration front capture the essence of the physics of convective transport in a capillary in the viscous limit.

[1] P. Friedlingstein, M. W. Jones, M. O'Sullivan, R. M. Andrew, D. C. Bakker, J. Hauck, C. Le Quéré, G. P. Peters, W. Peters, J. Pongratz *et al.*, Global carbon budget 2021, Earth Syst. Sci. Data **14**, 1917 (2022).

[2] R.-P. Ye, J. Ding, W. Gong, M. D. Argyle, Q. Zhong, Y. Wang, C. K. Russell, Z. Xu, A. G. Russell, Q. Li *et al.*, CO_2 hydrogenation to high-value products via heterogeneous catalysis, Nat. Commun. **10**, 5698 (2019).

[3] H. Hassanzadeh, M. Pooladi-Darvish, and D. W. Keith, Scaling behavior of convective mixing, with application to geological storage of CO_2, AIChE J. **53**, 1121 (2007).

[4] H. Emami-Meybodi, H. Hassanzadeh, C. P. Green, and J. Ennis-King, Convective dissolution of CO_2 in saline aquifers: Progress in modeling and experiments, Int. J. Greenhouse Gas Control **40**, 238 (2015).

[5] M. De Paoli, Influence of reservoir properties on the dynamics of a migrating current of carbon dioxide, Phys. Fluids **33**, 016602 (2021).

[6] S. Backhaus, K. Turitsyn, and R. E. Ecke, Convective instability and mass transport of diffusion layers in a Hele-Shaw geometry, Phys. Rev. Lett. **106**, 104501 (2011).

[7] V. Loodts, L. Rongy, and A. De Wit, Impact of pressure, salt concentration, and temperature on the convective dissolution of carbon dioxide in aqueous solutions, Chaos **24**, 043120 (2014).

[8] B. Wen, D. Akhbari, L. Zhang, and M. A. Hesse, Convective carbon dioxide dissolution in a closed porous medium at low pressure, J. Fluid Mech. **854**, 56 (2018).

[9] M. C. Rogers and S. W. Morris, Buoyant plumes and vortex rings in an autocatalytic chemical reaction, Phys. Rev. Lett. **95**, 024505 (2005).

[10] V. Loodts, H. Saghou, B. Knaepen, L. Rongy, and A. De Wit, Differential diffusivity effects in reactive convective dissolution, Fluids **3**, 83 (2018).

[11] Y. Gu, V. Hegde, and K. J. Bishop, Measurement and mitigation of free convection in microfluidic gradient generators, Lab Chip **18**, 3371 (2018).

[12] F. Sepahi, N. Pande, K. L. Chong, G. Mul, R. Verzicco, D. Lohse, B. T. Mei, and D. Krug, The effect of buoyancy driven convection on the growth and dissolution of bubbles on electrodes, Electrochim. Acta **403**, 139616 (2022).

[13] E. Dietrich, S. Wildeman, C. W. Visser, K. Hofhuis, E. S. Kooij, H. J. W. Zandvliet, and D. Lohse, Role of natural convection in the dissolution of sessile droplets, J. Fluid Mech. **794**, 45 (2016).

[14] K. L. Chong, Y. Li, C. S. Ng, R. Verzicco, and D. Lohse, Convection-dominated dissolution for single and multiple immersed sessile droplets, J. Fluid Mech. **892**, A21 (2020).

[15] O. R. Enríquez, C. Sun, D. Lohse, A. Prosperetti, and D. Van Der Meer, The quasi-static growth of CO_2 bubbles, J. Fluid Mech. **741**, R1 (2014).

[16] Á. Moreno Soto, O. R. Enríquez, A. Prosperetti, D. Lohse, and D. van der Meer, Transition to convection in single bubble diffusive growth, J. Fluid Mech. **871**, 332 (2019).

[17] H. Hassanzadeh, M. Pooladi-Darvish, and D. W. Keith, The effect of natural flow of aquifers and associated dispersion on the onset of buoyancy-driven convection in a saturated porous medium, AIChE J. **55**, 475 (2009).

[18] Y. Gholami, R. Azin, R. Fatehi, S. Osfouri, and A. Bahadori, Prediction of carbon dioxide dissolution in bulk water under isothermal pressure decay at different boundary conditions, J. Mol. Liq. **202**, 23 (2015).

[19] Y. Tang, Z. Li, R. Wang, M. Cui, X. Wang, Z. Lun, and Y. Lu, Experimental study on the density-driven carbon dioxide convective diffusion in formation water at reservoir conditions, ACS Omega **4**, 11082 (2019).

[20] F. Du, H. Ma, and Y. Gu, Three different periods of CO_2 dissolution into a light crude oil, Can. J. Chem. Eng. **97**, 330 (2019).

[21] H. Karimaie and E. Lindeberg, Experimental verification of CO_2 dissolution rate due to diffusion induced convection, Energy Procedia **114**, 4917 (2017).
[22] R. Farajzadeh, P. L. Zitha, and J. Bruining, Enhanced mass transfer of CO_2 into water: Experiment and modeling, Ind. Eng. Chem. Res. **48**, 6423 (2009).
[23] M. De Paoli, F. Zonta, and A. Soldati, Dissolution in anisotropic porous media: Modelling convection regimes from onset to shutdown, Phys. Fluids **29**, 026601 (2017).
[24] M. C. Kim, K. H. Song, C. K. Choi, and J.-K. Yeo, Onset of buoyancy-driven convection in a liquid-saturated cylindrical porous layer supported by a gas layer, Phys. Fluids **20**, 054104 (2008).
[25] O. Shishkina, Rayleigh-Bénard convection: The container shape matters, Phys. Rev. Fluids **6**, 090502 (2021).
[26] R. N. Moghaddam, B. Rostami, P. Pourafshary, and Y. Fallahzadeh, Quantification of density-driven natural convection for dissolution mechanism in CO_2 sequestration, Transp. Porous Media **92**, 439 (2012).
[27] P. Yang, H. Guo, Z. Wang, and Q. Zhou, Density and volumetric properties of binary mixtures of CO_2+ hexadecane from (303.2 to 473.2) K and pressures up to 50.0 MPa, J. Chem. Eng. Data **64**, 2568 (2019).
[28] R. Zhao, M. Xu, J. Yang, J. Y. Fu, M. Heng, and X.-a. Yue, Non-constant diffusion behavior for CO_2 diffusion into brine: Influence of density-driven convection, J. Solution Chem. **47**, 1926 (2018).
[29] M. J. Doughty, ph dependent spectral properties of sodium fluorescein ophthalmic solutions revisited, Ophthalmic Physiol. Opt. **30**, 167 (2010).
[30] T. A. Robertson, F. Bunel, and M. S. Roberts, Fluorescein derivatives in intravital fluorescence imaging, Cells **2**, 591 (2013).
[31] S. Yewalkar, T. Wu, D. Kuan, H. Wang, D. Li, A. Johnson, D. Posarac, S. Duff, and X. T. Bi, Applicability of differential fluorescein diacetate and propidium iodide fluorescence staining for monitoring algal growth and viability, Waste Disposal Sustainable Energy **1**, 199 (2019).
[32] D. P. Faasen, F. Sepahi, D. Krug, R. Verzicco, P. Peñas, D. Lohse, and D. van der Meer, Diffusive and convective dissolution of carbon dioxide in a vertical cylindrical cell, Phys. Rev. Fluids **8**, 093501 (2023).
[33] D. P. Faasen, D. van der Meer, D. Lohse, and P. Peñas, Slug bubble growth and dissolution by solute exchange, Phys. Rev. Fluids **6**, 113501 (2021).
[34] G. Ahlers, E. Bodenschatz, R. Hartmann, X. He, D. Lohse, P. Reiter, R. J. A. M. Stevens, R. Verzicco, M. Wedi, S. Weiss, R. Verzicco, M. Wedi, S. Weiss, X. Zhang, L. Zwirner, and O. Shishkina, Aspect ratio dependence of heat transfer in a cylindrical Rayleigh-Bénard cell, Phys. Rev. Lett. **128**, 084501 (2022).
[35] O. R. Enríquez, C. Hummelink, G.-W. Bruggert, D. Lohse, A. Prosperetti, D. van der Meer, and C. Sun, Growing bubbles in a slightly supersaturated liquid solution, Rev. Sci. Instrum. **84**, 065111 (2013).
[36] M. Raffel, C. E. Willert, F. Scarano, C. J. Kähler, S. T. Wereley, and J. Kompenhans, *Particle Image Velocimetry: A Practical Guide* (Springer, Cham, Switzerland, 2018).
[37] B.-S. Chun and G. T. Wilkinson, Interfacial tension in high-pressure carbon dioxide mixtures, Ind. Eng. Chem. Res. **34**, 4371 (1995).
[38] N. Pande, S. K. Chandrasekar, D. Lohse, G. Mul, J. A. Wood, B. T. Mei, and D. Krug, Electrochemically induced pH change: Time-resolved confocal fluorescence microscopy measurements and comparison with numerical model, J. Phys. Chem. Lett. **11**, 7042 (2020).
[39] R. Sander, Compilation of Henry's law constants (version 4.0) for water as solvent, Atmos. Chem. Phys. **15**, 4399 (2015).
[40] A. Tamimi, E. B. Rinker, and O. C. Sandall, Diffusion coefficients for hydrogen sulfide, carbon dioxide, and nitrous oxide in water over the temperature range 293-368 K, J. Chem. Eng. Data **39**, 330 (1994).
[41] G. I. Taylor, Dispersion of soluble matter in solvent flowing slowly through a tube, Proc. R. Soc. London A **219**, 186 (1953).
[42] R. Aris, On the dispersion of a solute in a fluid flowing through a tube, Proc. R. Soc. London A **235**, 67 (1956).
[43] R. B. Bird, Transport phenomena, Appl. Mech. Rev. **55**, R1 (2002).
[44] B. Mazumder, Taylor diffusion for a natural convective flow through a vertical channel, Int. J. Eng. Sci. **19**, 771 (1981).
[45] S. Chevalier, T. F. Faisal, Y. Bernabe, R. Juanes, and M. Sassi, Numerical sensitivity analysis of density

driven CO_2 convection with respect to different modeling and boundary conditions, Heat Mass Transfer **51**, 941 (2015).
[46] G. Taylor, Diffusion and mass transport in tubes, Proc. Phys. Soc. Sec. B **67**, 857 (1954).
[47] S. Grossmann and D. Lohse, Scaling in thermal convection: A unifying theory, J. Fluid Mech. **407**, 27 (2000).
[48] S. Grossmann and D. Lohse, Thermal convection for large Prandtl numbers, Phys. Rev. Lett. **86**, 3316 (2001).
[49] G. Ahlers, S. Grossmann, and D. Lohse, Heat transfer and large scale dynamics in turbulent Rayleigh-Bénard convection, Rev. Mod. Phys. **81**, 503 (2009).
[50] This estimate is consistent with the well-known relation $\mathrm{Sh}_d \sim \sqrt{\mathrm{Pe}}$, with the Sherwood and Péclet numbers defined as $\mathrm{Sh}_d = q''_{CO_2} d/(C_{\mathrm{sat}} D)$ and $\mathrm{Pe} = \bar{u} d/(2D)$.
[51] Taking the time derivative of the entire equation leads to the same conclusion under the assumption of a steady state $d^2\bar{u}/dt^2 = d\bar{u}/dt = 0$.
[52] H. Brenner and D. A. Edwards, *Macrotransport Processes* (Butterworth-Heinemann, Stoneham, MA, 1993).
[53] S. Vedel and H. Bruus, Transient Taylor–Aris dispersion for time-dependent flows in straight channels, J. Fluid Mech. **691**, 95 (2012).
[54] S. Marbach and K. Alim, Active control of dispersion within a channel with flow and pulsating walls, Phys. Rev. Fluids **4**, 114202 (2019).
[55] A. Vilquin, V. Bertin, P. Soulard, G. Guyard, E. Raphaël, F. Restagno, T. Salez, and J. D. McGraw, Time dependence of advection-diffusion coupling for nanoparticle ensembles, Phys. Rev. Fluids **6**, 064201 (2021).
[56] A. Vilquin, V. Bertin, E. Raphaël, D. S. Dean, T. Salez, and J. D. McGraw, Nanoparticle taylor dispersion near charged surfaces with an open boundary, Phys. Rev. Lett. **130**, 038201 (2023).
[57] One can show that x is the nontrivial ($x \neq 1$) solution of $x^4 - 3x^2 + 2 + 2\log x = 0$ and y is related to x by $y = x^2(2 - x^2)/(1 - x^2)^2$.